RESEARCH ARTICLE

Genetic Algorithm Based PFOID-SMC with a Sliding Mode Observer for a Quadcopter under Sensing and Communication Constraints

Nidhi Singh[1,*], **Prashant Nigam**[1] and **Lillie Dewan**[2]

[1] Department of Electrical Engineering, Gautam Buddha University, Greater Noida, Uttar Pradesh 201312, India
[2] Department of Electrical Engineering, National Institute of Technology Kurukshetra, Kurukshetra, Haryana 136119, India

Abstract

This paper presents a genetic algorithm (GA)-tuned sliding mode controller for a quadcopter (QuCo) in which the sliding surface is built from a proportional-fractional-order-integral-derivative (PFOID) error function (PFOID-SMC). The aim is to achieve accurate trajectory tracking in the presence of aerodynamic drag, wind, sensor noise and parametric uncertainty. Sensing and communication are kept inside the closed loop. The controller receives only measured or estimated states from a gyroscope (200 Hz), an attitude and heading reference system (100 Hz), an RTK-GNSS receiver (10 Hz) and a barometer (50 Hz), each with its own bias and noise, while the reference and the GNSS position are sent over a link with delay, packet loss and quantization. A sliding mode observer reconstructs attitude, angular rates, velocities, wind and disturbance accelerations and motor faults, and its disturbance estimates enter the equivalent control. Finite-time reaching and exponential convergence of the sliding variables are proved channel by channel with Lyapunov functions, and the stability of the complete cascade is checked numerically. The controller is compared with GA-tuned PID, conventional SMC, FOPID, super-twisting SMC and the earlier PFOID-SMC law in 15 scenarios, each with five noise realizations. In nominal conditions, it is not the most accurate (3-D position RMSE 0.119 m, against 0.071 m for FOPID). It gives the lowest error, however, under the strongest wind (0.134 m), under a 30 % increase in mass and inertia (0.179 m, against at least 0.82 m for all baselines) and after a 40 % loss of effectiveness of one motor (0.147 m). Without the observer, the same controller diverges.

Keywords: Genetic algorithm, fractional-order control, sliding mode control, sliding mode observer, parametric uncertainty, unmanned aerial vehicle, sensor modelling, networked control.

1 Introduction

Unmanned aerial vehicles (UAVs) are now used in a wide range of military and civilian tasks [1], including disaster relief, surveillance, precision agriculture, forest-fire fighting, aerial photography, geospatial mapping, industrial inspection, crop-disease

Submitted: 28 September 2026
Revised: 25 October 2026
Accepted: 28 October 2026
Published: 02 November 2026

Vol. 3, **No.** 4, 2026.
10.62762/TSCC.2026.637136

***Corresponding author:**
✉ Nidhi Singh
nidhi@gbu.ac.in

Citation
Singh, N., Nigam, P., & Dewan, L. (2026). Genetic Algorithm Based PFOID-SMC with a Sliding Mode Observer for a Quadcopter under Sensing and Communication Constraints. *ICCK Transactions on Sensing, Communication, and Control*, 3(4), 210–236.

© 2026 ICCK (Institute of Central Computation and Knowledge)

identification and logistics [2]. Of the many UAV configurations built for research, quadrotor platforms are the most common [3, 4]. Their popularity comes from a combination of autonomous flight, simple mechanical design, low cost, on-board cameras, high agility, stable hovering and vertical take-off and landing (VTOL) [5]. For these reasons the quadrotor, referred to here as QuCo, has become a focal point of recent research [6].

QuCos are used in health care, transportation and security, largely because their small size and high manoeuvrability allow them to carry out complex missions [7]. Controlling them is difficult. The QuCo is underactuated, and its rotational and translational dynamics are strongly coupled [8]. The dynamics are nonlinear and include gyroscopic and aerodynamic effects that matter even in hover [9]. Outdoors, the vehicle is also sensitive to external disturbances [10]. These difficulties have motivated a range of control techniques, including proportional-integral-derivative (PID) control, sliding mode control (SMC), the linear quadratic regulator (LQR) and backstepping [11].

Each of these methods has strengths and weaknesses. LQR requires an accurate dynamic model. SMC is robust to external perturbations and parameter variations, but its discontinuous switching can cause high-frequency chattering [12]. PID control is still dominant in industry because of its simple structure, its three easily tuned parameters and the fact that it needs no detailed plant model. It handles small uncertainties and perturbations well, but its performance degrades under large, time-varying uncertainties and disturbances [13].

Because PID control is easy to implement on low-cost, energy-efficient hardware, it remains attractive for quadrotor UAVs. Fractional-order (FO) calculus adds tuning freedom to the PID structure and has been widely applied to nonlinear systems, mainly because FO controllers are less sensitive to disturbances and parameter changes [14]. Efe [15] replaced the reaching dynamics of an integral sliding mode controller by a fractional-order law and reported a markedly more robust response than its integer-order counterpart. Izaguirre-Espinosa et al. [16] enforced the sliding manifold through a fractional-order reaching phase for quadrotor attitude control and validated the finite-time convergence experimentally, while Shi et al. [17] combined a fractional-order sliding surface with backstepping and reported reduced chattering under uncertain disturbances. Labbadi et al. [18] added a continuous fractional-order super-twisting term to a PID sliding surface for path following, and Pazooki and Mazinan [19] tuned a fuzzy sliding mode controller for a quadrotor with a genetic algorithm.

Kumar and Dewan [20] proposed a hybrid sliding mode-backstepping controller (SMCBS) with a PFOID surface for a QuCo flying in a disturbed environment, and in [21] they stabilized the vehicle under disturbances and mass variation with a hybrid controller. Abro and Abdallah [22] used fractional-order control to improve the transient response and reduce overshoot in helical trajectory tracking of multi-agent quadrotors. Nguyen et al. [23] designed an SMC trajectory-tracking controller and reported small tracking errors under external disturbances. Shui and Peng [24] tuned ADRC parameters with an improved GA, and Li et al. [25] used a dual-loop scheme in which a GA-PSO-optimized PID controller regulates position and a fuzzy-tuned linear ADRC stabilizes attitude. Super-twisting control of quadrotor attitude was demonstrated in [26], and finite-time adaptive SMC under unknown disturbances and actuator constraints in [27]. Khaled and Boumehraz [28] combined an adaptive sliding mode controller with an observer for quadrotor altitude and attitude control.

Two gaps remain in these studies, including the PFOID-SMC of [29]. First, the controllers are designed and validated with the true state in the feedback path. Sensing is represented at most by additive noise, and the link between the ground station and the vehicle is ignored, although in practice set-points and positioning data arrive with latency and packet loss [30]. Second, the gains are usually chosen by trial and error, and robustness claims are seldom backed by explicit disturbance, fault and uncertainty profiles or by repeated tuning runs.

To address these gaps, this paper embeds a GA-tuned PFOID-SMC in a sensing- and communication-aware closed loop. The fractional-order surface is combined with sliding mode control to improve robustness against external disturbances and model uncertainty. Compared with the PFOID-SMC of [29], the paper makes five contributions.

(1) Every on-board sensor is modelled with its own sampling rate, bias and noise, and the controller uses only measured or estimated states.

(2) A super-twisting/higher-order sliding mode observer (SMO) estimates attitude, rates,

velocities, wind and disturbance accelerations and the loss of effectiveness of each motor. Its disturbance estimates are fed to the equivalent control.

(3) Delay, jitter, packet loss, quantization and a reduced update rate are applied to the reference and GNSS links.

(4) The reaching law of [29], which lacks damping, is replaced by a damped law. The Lyapunov cross terms are bounded explicitly, and the type of convergence is stated for each signal.

(5) The GA is repeated with ten random seeds and validated on a trajectory not used for tuning, and all baselines are tuned with the same objective, budget and bounds.

The rest of the paper is organized as follows. Section 2 presents the QuCo model with disturbances, the sensing and communication models, the SMO, the controller and its stability analysis. Section 3 reports and discusses the simulation results, and Section 4 concludes the paper.

2 Modelling and Control Design

Figure 1 shows the QuCo with the earth frame E and the body frame B. The vehicle has six degrees of freedom: the position $[x, y, z]^T$ of its centre of gravity in E and the roll, pitch and yaw angles (ϕ, θ, ψ) [31, 32]. The linear velocity in E is $[\dot{x}, \dot{y}, \dot{z}]^T$. The motion is produced by the lift forces $F_1, \ldots, F_4$ of the four rotors, each proportional to the square of the rotor speed.

Applying the Euler-Lagrange formalism gives the dynamic model [33, 34]

$$\begin{aligned}
\ddot{x} &= \tfrac{1}{m}(\cos\phi\sin\theta\cos\psi + \sin\phi\sin\psi)V_1,\\
\ddot{y} &= \tfrac{1}{m}(\cos\phi\sin\theta\sin\psi - \sin\phi\cos\psi)V_1,\\
\ddot{z} &= \tfrac{V_1}{m}\cos\phi\cos\theta - g,\\
\ddot{\phi} &= \dot{\theta}\dot{\psi}\tfrac{J_{yy}-J_{zz}}{J_{xx}} + \tfrac{J_r}{J_{xx}}\dot{\theta}\,\omega_r + \tfrac{l}{J_{xx}}V_2,\\
\ddot{\theta} &= \dot{\phi}\dot{\psi}\tfrac{J_{zz}-J_{xx}}{J_{yy}} - \tfrac{J_r}{J_{yy}}\dot{\phi}\,\omega_r + \tfrac{l}{J_{yy}}V_3,\\
\ddot{\psi} &= \dot{\phi}\dot{\theta}\tfrac{J_{xx}-J_{yy}}{J_{zz}} + \tfrac{1}{J_{zz}}V_4,
\end{aligned} \tag{1}$$

where m is the mass, J_{xx}, J_{yy}, J_{zz} are the moments of inertia, J_r is the rotor inertia, l is the arm length, g is the gravitational acceleration and ω_r is the relative rotor speed. V_1 is the total thrust, $V_2 = F_4 - F_2$ and $V_3 = F_3 - F_1$ are the roll and pitch inputs, and $V_4 = (k_m/b)(-F_1 + F_2 - F_3 + F_4)$ is the yaw moment, with $F_i = b\,\omega_i^2$ $(i = 1, \ldots, 4)$, b the lift coefficient and ω_i the speed of rotor i [35]. The numerical values are listed in Table 2.

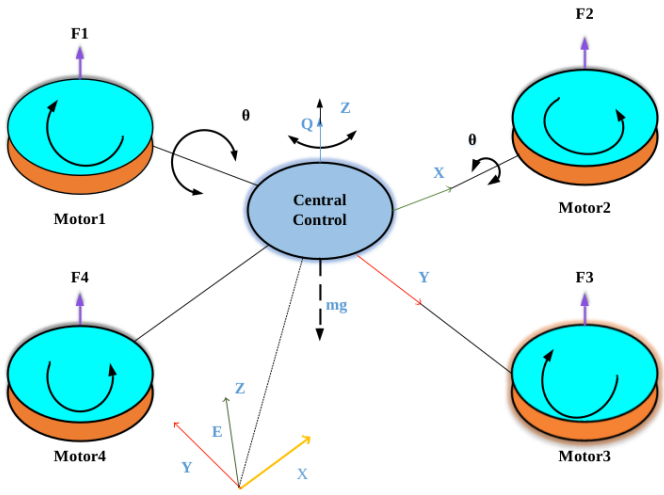


Figure 1. QuCo model with the earth frame E and body frame B.

2.1 Uncertainty, disturbances and actuator faults

Variations in mass, blade length, inertia and aerodynamic coefficients give rise to parametric uncertainty, to which many classical controllers are not robust. Let d_i^{ext} denote the total external disturbance (wind, external noise and sensor noise) and d_i^{PU} the effect of parametric uncertainty, $i \in \{x, y, z, \phi, \theta, \psi\}$.

Wind, external noise, sensor noise and aerodynamic effects are treated as disturbances, whereas changes in the QuCo parameters are treated as parametric uncertainty. The aerodynamic effect is caused by air friction and has two parts, drag forces and drag moments [36]. The drag force opposes the motion and grows with the vehicle velocity, and the drag moment acts on the body. Both depend on the propeller design and the air density. Sensor noise enters through the measurements used for feedback and appears as random noise, while external noise acts directly on the six degrees of freedom [33]. Wind disturbance arises in open environments, where sudden changes in wind speed can destabilize the vehicle; it is represented by additional forces and moments. Figure 2 summarizes these disturbances.

A sliding mode observer can use sensor data to detect and reconstruct actuator faults and pass them to a sliding-mode fault-tolerant controller [37]. Such a design does not rely on precise fault estimates. It redistributes the control effort to the healthy actuators so that the control objective is still met. The observer used in this paper is designed in Section 2.5. Adding

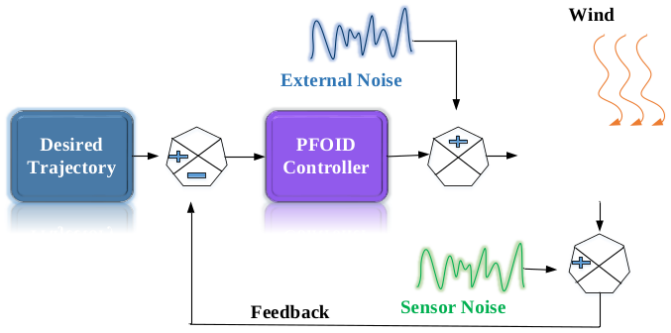


Figure 2. Disturbances acting on the QuCo model.

the disturbance terms and the unknown actuator faults ε_{V_k} $(k = 1, \ldots, 4)$ to (1) gives [38]

$$\begin{aligned}
\ddot{x} &= \tfrac{1}{m}(\cos\phi\sin\theta\cos\psi + \sin\phi\sin\psi)(V_1 + \varepsilon_{V_1}) \\
&\quad + d_x^{PU} + d_x^{ext}, \\
\ddot{y} &= \tfrac{1}{m}(\cos\phi\sin\theta\sin\psi - \sin\phi\cos\psi)(V_1 + \varepsilon_{V_1}) \\
&\quad + d_y^{PU} + d_y^{ext}, \\
\ddot{z} &= \tfrac{V_1+\varepsilon_{V_1}}{m}\cos\phi\cos\theta - g + d_z^{PU} + d_z^{ext}, \\
\ddot{\phi} &= \dot{\theta}\dot{\psi}\tfrac{J_{yy}-J_{zz}}{J_{xx}} + \tfrac{J_r}{J_{xx}}\dot{\theta}\,\omega_r + \tfrac{l}{J_{xx}}(V_2 + \varepsilon_{V_2}) \\
&\quad + d_\phi^{PU} + d_\phi^{ext}, \\
\ddot{\theta} &= \dot{\phi}\dot{\psi}\tfrac{J_{zz}-J_{xx}}{J_{yy}} - \tfrac{J_r}{J_{yy}}\dot{\phi}\,\omega_r + \tfrac{l}{J_{yy}}(V_3 + \varepsilon_{V_3}) \\
&\quad + d_\theta^{PU} + d_\theta^{ext}, \\
\ddot{\psi} &= \dot{\phi}\dot{\theta}\tfrac{J_{xx}-J_{yy}}{J_{zz}} + \tfrac{1}{J_{zz}}(V_4 + \varepsilon_{V_4}) + d_\psi^{PU} + d_\psi^{ext}.
\end{aligned} \tag{2}$$

Here V_1 is the thrust input and V_2, V_3, V_4 are the roll, pitch and yaw inputs. In state-space form,

$$\dot{Y} = h(Y, V) + D(Y, V), \tag{3}$$

where D is the disturbance, $V = [V_1, V_2, V_3, V_4]^T$ is the input vector and $Y = [y_1, \ldots, y_{12}]^T = [\phi, \dot{\phi}, \theta, \dot{\theta}, \psi, \dot{\psi}, z, \dot{z}, x, \dot{x}, y, \dot{y}]^T \in \mathbb{R}^{12}$. With $\dot{y}_{2k-1} = y_{2k}$ $(k = 1, \ldots, 6)$, the remaining equations of (2) read

$$\begin{aligned}
\dot{y}_2 &= b_1 y_4 y_6 + b_2 y_4 \omega_r + c_1(V_2 + \varepsilon_{V_2}) + d_\phi, \\
\dot{y}_4 &= b_3 y_2 y_6 + b_4 y_2 \omega_r + c_2(V_3 + \varepsilon_{V_3}) + d_\theta, \\
\dot{y}_6 &= b_5 y_2 y_4 + c_3(V_4 + \varepsilon_{V_4}) + d_\psi, \\
\dot{y}_8 &= -g + \tfrac{1}{m}\cos y_1 \cos y_3\,(V_1 + \varepsilon_{V_1}) + d_z, \\
\dot{y}_{10} &= \tfrac{1}{m} v_x (V_1 + \varepsilon_{V_1}) + d_x, \\
\dot{y}_{12} &= \tfrac{1}{m} v_y (V_1 + \varepsilon_{V_1}) + d_y,
\end{aligned} \tag{4}$$

where $d_x, \ldots, d_\psi$ are the total disturbances (external disturbance plus parametric uncertainty), $b_1 = (J_{yy} - J_{zz})/J_{xx}$, $b_2 = J_r/J_{xx}$, $b_3 = (J_{zz} - J_{xx})/J_{yy}$, $b_4 = -J_r/J_{yy}$, $b_5 = (J_{xx} - J_{yy})/J_{zz}$, $c_1 = l/J_{xx}$, $c_2 = l/J_{yy}$, $c_3 = 1/J_{zz}$, and the virtual inputs are

$$\begin{aligned}
v_x &= \cos y_1 \sin y_3 \cos y_5 + \sin y_1 \sin y_5, \\
v_y &= \cos y_1 \sin y_3 \sin y_5 - \sin y_1 \cos y_5.
\end{aligned} \tag{5}$$

Each disturbance is bounded, $|d_j| \le D_j^+$, where D_j^+ is a positive constant and $j \in \{x, y, z, \phi, \theta, \psi\}$.

2.2 Actuator model and common channel form

The control inputs of (1) are related to the rotor thrusts $F_i = b\,\omega_i^2$ by

$$\begin{aligned}
&V_1 = \textstyle\sum_{i=1}^4 F_i, \quad V_2 = F_4 - F_2, \quad V_3 = F_3 - F_1, \\
&V_4 = \tfrac{k_m}{b}(-F_1 + F_2 - F_3 + F_4), \\
&\omega_r = -\omega_1 + \omega_2 - \omega_3 + \omega_4,
\end{aligned} \tag{6}$$

where k_m is the drag-moment coefficient. Equation (6) is written as $\mathbf{V} = \mathbf{A}\mathbf{F}$ and inverted on board to obtain the commanded thrusts, which are saturated to $0 \le F_{i,c} \le F_{\max}$. Each rotor responds with a first-order lag,

$$\begin{aligned}
&\tau_m \dot{\omega}_i = \sqrt{F_{i,c}/b} - \omega_i, \\
&F_i = \big(1 - \rho_i(t)\big) b\,\omega_i^2, \quad 0 \le \rho_i(t) < 1,
\end{aligned} \tag{7}$$

where τ_m is the rotor time constant and ρ_i the loss of effectiveness (LOE) of motor i ($\rho_i = 0$ for a healthy motor). The drag moment of a faulty rotor is scaled by the same factor.

Aerodynamic drag, wind, external torques, parametric uncertainty (PU) and actuator faults act on the vehicle [36, 38]. With the wind velocity $\mathbf{w} = [w_x, w_y, w_z]^T$, the translational drag constants $K_{t,i}$, the rotational drag constants $K_{r,i}$ and the external torques $\tau_{e,j}$, every channel of (1) can be written in the common form

$$\ddot{y}_j = f_j(\mathbf{Y}) + g_j\,u_j + d_j(t), \quad j \in \{x, y, z, \phi, \theta, \psi\}, \tag{8}$$

with the nominal drifts and input gains

$$\begin{aligned}
&f_x = -\tfrac{K_{t,x}}{m}\dot{x}, \quad f_y = -\tfrac{K_{t,y}}{m}\dot{y}, \quad f_z = -\tfrac{K_{t,z}}{m}\dot{z}, \\
&f_\phi = \dot{\theta}\dot{\psi}\,b_1 + \dot{\theta}\,\omega_r b_2 - \tfrac{K_{r,x}}{J_{xx}}\dot{\phi}, \\
&f_\theta = \dot{\phi}\dot{\psi}\,b_3 + \dot{\phi}\,\omega_r b_4 - \tfrac{K_{r,y}}{J_{yy}}\dot{\theta}, \\
&f_\psi = \dot{\phi}\dot{\theta}\,b_5 - \tfrac{K_{r,z}}{J_{zz}}\dot{\psi}, \quad g_x = g_y = g_z = 1, \\
&g_\phi = \tfrac{l}{J_{xx}}, \quad g_\theta = \tfrac{l}{J_{yy}}, \quad g_\psi = \tfrac{1}{J_{zz}},
\end{aligned} \tag{9}$$

where b_1-b_5 are as defined after (4). The rotational inputs are $u_\phi = V_2$, $u_\theta = V_3$ and $u_\psi = V_4$, and the translational inputs are the virtual accelerations

$$\begin{aligned}
&U_x = \tfrac{V_1}{m}(c_\phi s_\theta c_\psi + s_\phi s_\psi), \quad U_y = \tfrac{V_1}{m}(c_\phi s_\theta s_\psi - s_\phi c_\psi), \\
&U_z = \tfrac{V_1}{m} c_\phi c_\theta - g,
\end{aligned} \tag{10}$$

with $c_{(\cdot)} = \cos(\cdot)$ and $s_{(\cdot)} = \sin(\cdot)$. The lumped disturbance d_j collects the wind-induced drag

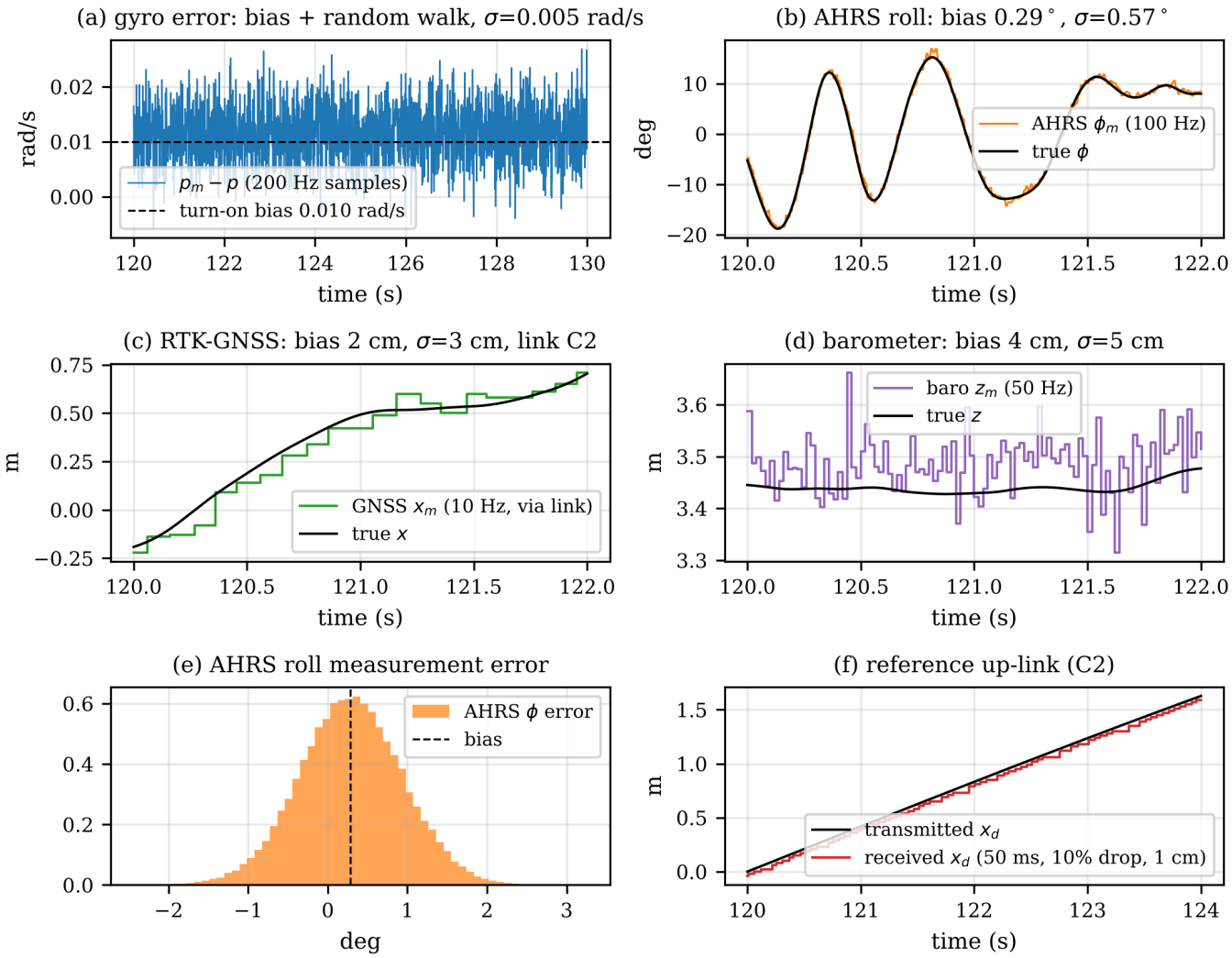


Figure 3. Sensor and link models in the loop (Comm. C2 run, proposed controller): (a) gyroscope error with turn-on bias and random walk; (b) AHRS roll angle versus truth; (c) 10 Hz GNSS samples received over the link; (d) barometer; (e) histogram of the AHRS roll error with its bias; (f) transmitted and received reference (50 ms delay, 10 % drop, 1 cm quantization).

$K_{t,j}w_j/m$, the external torques $\tau_{e,j}/J_j$, the effect of mass and inertia uncertainty, the LOE faults ρ_i and the unmodelled rotor lag. It is assumed bounded with a bounded derivative, $|d_j| \le D_j$ and $|\dot{d}_j| \le L_j$, which holds for every profile used here. The wind, gust, torque, uncertainty and fault profiles are defined in Section 3.1.

2.3 On-board sensing model

The controller has no access to the true state. Each sensor s is sampled at its own rate f_s and held constant between samples (zero-order hold):

$$\begin{aligned} &\mathbf{y}_s(t) = \mathbf{h}_s(\mathbf{X}(t_k)) + \mathbf{b}_s(t_k) + \mathbf{n}_s(t_k), \\ &t_k \le t < t_k + 1/f_s, \quad \dot{\mathbf{b}}_s = \mathbf{w}_{b,s}, \quad \mathbf{n}_s \sim \mathcal{N}(\mathbf{0}, \sigma_s^2 \mathbf{I}), \end{aligned} \tag{11}$$

where $\mathbf{b}_s$ is the sensor bias (a constant turn-on value plus, for the gyroscope, a random walk driven by $\mathbf{w}_{b,s}$) and $\mathbf{n}_s$ is white measurement noise. The gyroscope measures the body rates, $\mathbf{h}_{gyro} = \mathbf{W}(\phi,\theta)[\dot{\phi},\dot{\theta},\dot{\psi}]^T$, with

$$\mathbf{W}(\phi,\theta) = \begin{bmatrix} 1 & 0 & -\sin\theta \\ 0 & \cos\phi & \sin\phi\cos\theta \\ 0 & -\sin\phi & \cos\phi\cos\theta \end{bmatrix}, \tag{12}$$

and the on-board software converts them to Euler-angle rates using the estimated attitude. The attitude and heading reference system (AHRS) provides (ϕ,θ,ψ), the RTK-GNSS receiver provides (x,y) and the barometer provides z. The sampling rates, biases and noise levels (Section 3.1) are typical of low-cost MEMS IMU, RTK-GNSS and barometric hardware. Figure 3 shows sample signals from these models in the loop.

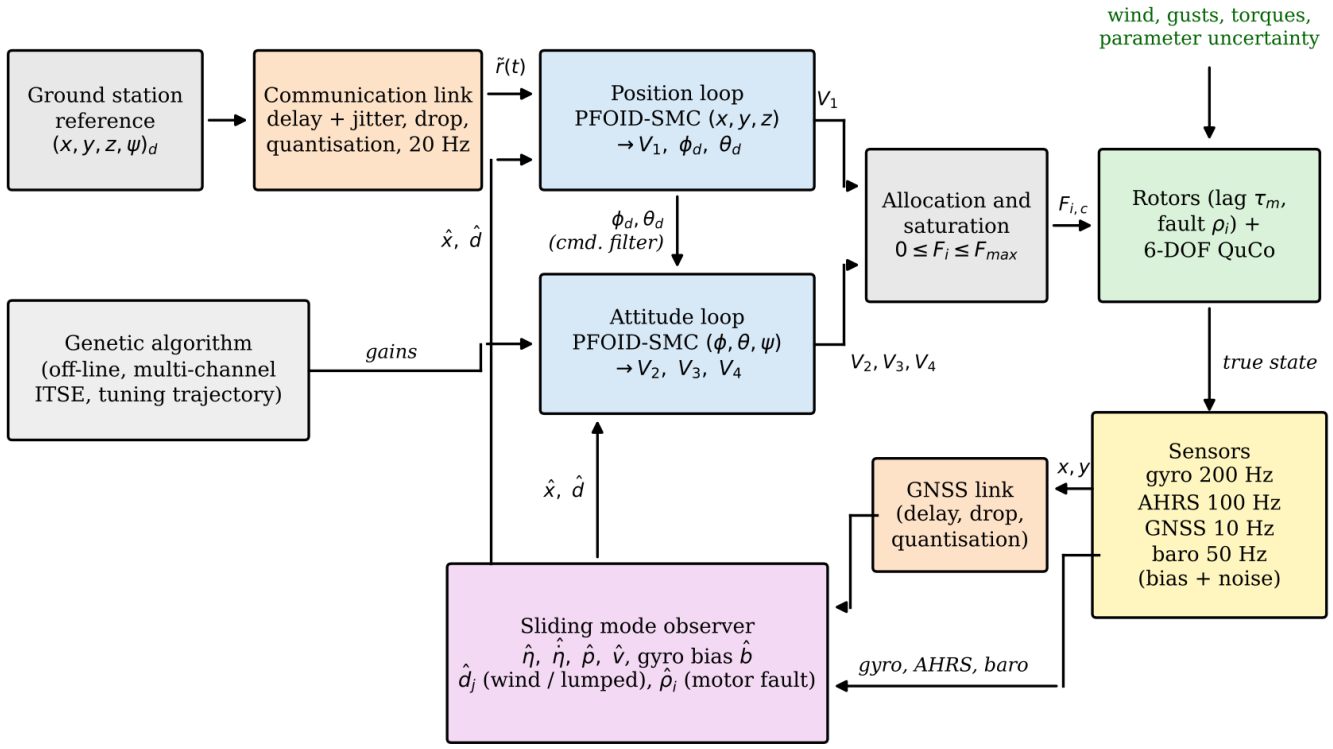


Figure 4. Sensing- and communication-aware closed loop: ground-station reference over a lossy link, PFOID-SMC position and attitude loops, allocation and saturation, rotors and plant with disturbances and faults, on-board sensors, GNSS link and sliding mode observer. The GA tunes the gains off-line.

2.4 Communication channel model

The desired trajectory $\mathbf{r}(t) = [x_d, y_d, z_d, \psi_d]^T$ and its first two derivatives are streamed from the ground station at $f_c = 20$ Hz, and the GNSS position reaches the flight computer over the same type of link. Packet k, generated at $t_k = k/f_c$, arrives with probability $1-p$ ($\nu_k \in \{0, 1\}$, Bernoulli), after the random delay $\tau_k = \bar{\tau}+\mathcal{U}(0, \tau_J)$, and carries positions quantized as $Q_q(r) = q\ \mathrm{round}(r/q)$ with $q = 0.01$ m. The receiver holds the newest packet that has arrived:

$$\tilde{\mathbf{r}}(t) = Q_q\big(\mathbf{r}(t_{k^*})\big), \quad k^* = \max\{k : \nu_k = 1,\ t_k+\tau_k \le t\}. \tag{13}$$

The mean delay $\bar{\tau}$, the jitter τ_J and the drop probability p define the communication levels of Section 3.1. Tracking errors are always computed against the true (transmitted) reference and the true vehicle state, so the cost of the link appears in every metric.

Both links are made communication-aware on board. Each packet carries its generation time, so the received set-point is extrapolated to the current time with its own derivatives, $\tilde{\mathbf{r}} + \dot{\tilde{\mathbf{r}}}\Delta + \frac{1}{2}\ddot{\tilde{\mathbf{r}}}\Delta^2$ with $\Delta = t - t_{k^*}$. The time-stamped GNSS sample is predicted forward with the current velocity estimate before it enters the observer innovation (Section 2.5.2). Neither mechanism is active when the link is ideal.

2.5 Sliding mode observer design

Sliding mode observers that reconstruct actuator faults for fault-tolerant SMC have been validated in hardware-in-the-loop experiments [37]. Here the observer runs at 1 kHz on the held measurements and uses the rotor-lag-filtered commanded inputs $\bar{u}_j$, which are known on board. Its outputs are the estimates $\hat{\boldsymbol{\eta}} = (\hat{\phi}, \hat{\theta}, \hat{\psi})$, $\dot{\hat{\boldsymbol{\eta}}}$, $\hat{\mathbf{p}}$, $\hat{\mathbf{v}}$, $\hat{d}_j$ and $\hat{\rho}_i$ (Figure 4).

2.5.1 *Attitude channels: super-twisting observer with bias correction*

For $j \in \{\phi, \theta, \psi\}$, let ω_j be the Euler-rate measurement obtained from the gyroscope through $\mathbf{W}^{-1}(\hat{\phi}, \hat{\theta})$ and let $\eta_{m,j}$ be the AHRS angle. With the innovations $e_{v,j} = \omega_j - \hat{b}_j - \hat{v}_j$ and $e_{q,j} = \eta_{m,j} - \hat{\eta}_j$, the observer is

$$\begin{aligned} \dot{\hat{v}}_j &= f_j(\hat{\boldsymbol{\eta}}, \hat{\mathbf{v}}) + g_j \bar{u}_j + \hat{d}_j \\ &\quad + k_1 |e_{v,j}|^{1/2} \operatorname{sign}(e_{v,j}), \\ \dot{\hat{d}}_j &= k_2 \operatorname{sign}(e_{v,j}), \\ \dot{\hat{\eta}}_j &= \hat{v}_j + l_q\, e_{q,j}, \qquad \dot{\hat{b}}_j = -l_b\, e_{q,j}, \end{aligned} \tag{14}$$

with $k_1 = 1.5\sqrt{L_a}$, $k_2 = 1.1L_a$, $L_a = 100$, $l_q = 4\ \mathrm{s}^{-1}$ and $l_b = 0.5\ \mathrm{s}^{-2}$. The first two equations form the super-twisting algorithm, whose internal state $\hat{v}_j$ is used only to extract the disturbance. The rate passed to the controller is the bias-corrected gyroscope rate $\dot{\hat{\eta}}_j = \omega_j - \hat{b}_j$, which keeps the high bandwidth of the gyroscope. If L_a exceeds the Lipschitz bound of d_j, the rate error $e_{v,j}$ and the disturbance error $\tilde{d}_j = d_j - \hat{d}_j$ converge to zero in finite time in the noise-free, continuous-time case [39, 40]. With sampled, noisy measurements they converge to a neighbourhood whose size scales with the noise level [41]. The last two equations fuse the AHRS angle and estimate the gyroscope bias: a residual bias makes $\hat{\eta}_j$ drift away from $\eta_{m,j}$, and $\hat{b}_j$ is driven until the drift vanishes.

2.5.2 *Translational channels: higher-order sliding mode observer*

Only position is measured, in x, y by GNSS (10 Hz) and in z by the barometer (50 Hz). For $j \in \{x, y, z\}$ and $e_{p,j} = p_{m,j} - \hat{p}_j$, a second-order robust exact differentiator with model input [41] is used:

$$\begin{aligned}
\dot{\hat{p}}_j &= \hat{v}_j + 2L_t^{1/3}|e_{p,j}|^{2/3}\,\mathrm{sign}(e_{p,j}),\\
\dot{\hat{v}}_j &= f_j(\hat{\mathbf{v}}) + \bar{U}_j + \hat{d}_j + 2.12\,L_t^{2/3}|e_{p,j}|^{1/3}\,\mathrm{sign}(e_{p,j}),\\
\dot{\hat{d}}_j &= 1.1\,L_t\,\mathrm{sign}(e_{p,j}),
\end{aligned} \tag{15}$$

with $L_t = 3\ \mathrm{m\,s}^{-3}$. When a GNSS sample taken at t_s is used at time t, the innovation is formed as $e_{p,j} = p_{m,j} + \hat{v}_j(t - t_s) - \hat{p}_j$, which removes the bias that a delayed measurement would otherwise inject into $\hat{d}_j$. $\bar{U}_j$ is obtained from (10) with the estimated attitude and the rotor-lag-filtered thrust. In the noise-free case the estimates converge in finite time; with noise of amplitude ε the accuracies are of order ε, $L_t^{1/3}\varepsilon^{2/3}$ and $L_t^{2/3}\varepsilon^{1/3}$ for position, velocity and disturbance [41]. The disturbance estimates are low-pass filtered ($\hat{d}_j^f$; 6 rad/s translational, 15 rad/s rotational) before the controller uses them.

2.5.3 *Actuator-fault reconstruction*

The filtered disturbance estimates of the z, ϕ, θ, ψ channels are mapped to an input residual and, through the inverse allocation of (6), to a per-motor thrust deficit:

$$\begin{aligned}
\Delta\hat{\mathbf{V}} &= \left[\frac{m\,\hat{d}_z^f}{\cos\hat{\phi}\cos\hat{\theta}},\ \frac{J_{xx}\hat{d}_\phi^f}{l},\ \frac{J_{yy}\hat{d}_\theta^f}{l},\ J_{zz}\hat{d}_\psi^f\right]^T,\\
\Delta\hat{\mathbf{F}} &= \mathbf{A}^{-1}\Delta\hat{\mathbf{V}}, \qquad \tau_\rho\dot{\hat{\rho}}_i = -\frac{\Delta\hat{F}_i}{\bar{F}_{i,c}} - \hat{\rho}_i,
\end{aligned} \tag{16}$$

with $\tau_\rho = 0.5$ s. The estimate $\hat{\rho}_i$ isolates and sizes the faulty motor (Section 3.3). Its effect on the control is already compensated through $\hat{d}_j$ in the equivalent control (Section 2.6.3), so the controller does not need the unknown fault magnitude, which would otherwise appear as a factor $(1 + \varepsilon)$ in the control law.

2.6 Controller design

Fractional-order PID controllers are widely used because, compared with integer-order PID, they can give a faster response with smaller oscillations and better robustness [42, 43]. This section develops a GA-tuned second-order SMC with a PFOID sliding surface for the 6-DOF QuCo and analyses its stability with Lyapunov functions.

2.6.1 *GA-tuned PFOID surface-based sliding mode controller*

The GA is used to tune the PFOID-SMC (proportional fractional-order integral-derivative second-order sliding mode control). The GA is a stochastic, population-based search method inspired by natural evolution; the fitness function evaluates each candidate after selection, crossover and mutation, which are the main stages of the algorithm [44]. The closed loop, including the sensor, communication and observer models, is simulated in a fixed-step discrete-time simulator (Section 3), and the design is assessed in terms of position, roll, pitch, yaw and altitude. Table 1 lists the GA settings.

Table 1. GA settings.

Parameter	Value
Population size	50
Number of generations	100 (5000 closed-loop evaluations per run)
Fitness function	ITSE + total variation of rotor thrusts, Eq. (28)
Selection	Normalized geometric ($q = 0.08$)
Crossover	Single point (probability 0.8)
Mutation	Uniform (probability 0.05 per gene)
Elitism	2 individuals
Encoding	Genes in $[0, 1]$; log scale for gains, linear for orders
Independent runs	10 seeds (proposed); 3 seeds per baseline, best retained

The PFOID-SMC uses a proportional fractional-order integral-derivative surface inside the SMC framework. The fractional-order integral term adds flexibility to the conventional PID surface. The control law has two parts: an equivalent control that linearizes the input-output map and a switching control that drives

the tracking error to zero. The inputs V_1-V_4 stabilize the altitude and the roll, pitch and yaw motions. For each channel,

$$u_j = u_{j,eq} + u_{j,sw}, \quad j \in \{x, y, z, \phi, \theta, \psi\}. \tag{17}$$

The equivalent control is derived for the nominal model ($D(Y, V) = 0$), and the switching control supplies extra effort against disturbances and unmodelled dynamics. PID-type and integral-type sliding surfaces with independent gains are common choices [45]. This paper uses the PFOID sliding surface of [29], defined by the first-order equation

$$\begin{aligned} &\dot{\delta}_j + \gamma_j \delta_j = \sigma_j = K_{Pj} e_j + K_{Ij}\, \mathcal{I}^{\vartheta_j} e_j + K_{Dj} \dot{e}_j, \\ &s_j = \dot{\delta}_j + \lambda_j \delta_j, \end{aligned} \tag{18}$$

where $\gamma_j, K_{Pj}, K_{Ij}, K_{Dj}, \lambda_j > 0$ are design constants and $\mathcal{I}^{\vartheta} e(t) = \frac{1}{\Gamma(\vartheta)} \int_0^t (t-\tau)^{\vartheta-1} e(\tau)\, d\tau$ is the fractional-order integral of order $0 < \vartheta < 1$; $\vartheta = 1$ recovers the PID surface. The derivative order is kept at unity so that the control input appears in $\dot{\sigma}_j$ with relative degree one. With a fractional derivative of order $\mu < 1$, $\dot{\sigma}_j$ would contain the input only through a fractional integral and the equivalent control could not be obtained. The auxiliary variable δ_j keeps the second-order sliding structure of [29, 46], and s_j is the sliding variable of the damped reaching law. The operators $\mathcal{I}^{\vartheta}$ and $\mathcal{D}^{1-\vartheta}$ are implemented with a ninth-order Oustaloup approximation on $[10^{-2}, 10^{2}]$ rad/s, discretized with the Tustin transform at the 200 Hz control rate [47]. Figure 5 shows the control structure.

2.6.2 Position control

Applying the law of Section 2.6.3 to $j \in \{x, y, z\}$ (with $g_j = 1$) gives the virtual accelerations U_x, U_y and U_z. From the third line of (10), the collective thrust is

$$V_1 = \frac{m(g + U_z)}{\cos\hat{\phi}\cos\hat{\theta}}. \tag{19}$$

Define $\mu_x = mU_x/V_1$ and $\mu_y = mU_y/V_1$, so that $\mu_x = c_\phi s_\theta c_\psi + s_\phi s_\psi$ and $\mu_y = c_\phi s_\theta s_\psi - s_\phi c_\psi$. Multiplying the first by s_ψ and the second by c_ψ and subtracting eliminates θ, because $\mu_x s_\psi - \mu_y c_\psi = s_\phi(s_\psi^2 + c_\psi^2) = s_\phi$. Multiplying by c_ψ and s_ψ and adding gives $\mu_x c_\psi + \mu_y s_\psi = c_\phi s_\theta$. The desired roll and pitch angles are therefore

$$\begin{aligned} \phi_d &= \arcsin(\mu_x \sin\hat{\psi} - \mu_y \cos\hat{\psi}), \\ \theta_d &= \arcsin\!\left(\frac{\mu_x \cos\hat{\psi} + \mu_y \sin\hat{\psi}}{\cos\phi_d}\right), \end{aligned} \tag{20}$$

with both arguments limited to $|\cdot| \le \sin 30^\circ$. The angles pass through a second-order command filter ($\omega_n = 25$ rad/s, $\zeta = 0.9$) that supplies $\dot{\phi}_d, \ddot{\phi}_d, \dot{\theta}_d, \ddot{\theta}_d$ to the attitude loop, while ψ_d and its derivatives come from the received reference (13).

2.6.3 Rotational control

The inputs V_j ($j = \phi, \theta, \psi$) control the rotational subsystem, and V_1 controls the translational subsystem. The same law is used for every channel of the common form (8), so the derivation below covers the roll, pitch and yaw channels and, with $g_j = 1$, the x, y and z channels of the position loop.

Differentiating (18) and using $\frac{d}{dt}\mathcal{I}^{\vartheta} e = \mathcal{D}^{1-\vartheta} e$ (zero initial conditions) together with (8) gives

$$\begin{aligned} \dot{\sigma}_j &= K_{Pj}\ddot{e}_j + K_{Ij}\mathcal{D}^{1-\vartheta_j} e_j \\ &\quad + K_{Dj}(\dddot{y}_{j,d} - f_j - g_j u_j - d_j), \\ \dot{s}_j &= \dot{\sigma}_j + (\lambda_j - \gamma_j)\dot{\delta}_j. \end{aligned} \tag{21}$$

The equivalent control uses the observer estimate $\hat{d}_j^f$, and the switching control uses a boundary layer of width Φ_j:

$$\begin{aligned} u_{j,eq} &= \frac{1}{g_j K_{Dj}}\Big[K_{Pj}\ddot{e}_j + K_{Ij}\mathcal{D}^{1-\vartheta_j} e_j + (\lambda_j - \gamma_j)\dot{\delta}_j \\ &\qquad + K_{Dj}\big(\dddot{y}_{j,d} - f_j(\hat{\mathbf{Y}}) - \hat{d}_j^f\big)\Big], \\ u_{j,sw} &= \frac{\beta_j s_j + K_{\delta j}\,\mathrm{sat}(s_j/\Phi_j)}{g_j K_{Dj}}. \end{aligned} \tag{22}$$

Substituting (22) into (21) gives the closed-loop sliding dynamics

$$\dot{s}_j = -\beta_j s_j - K_{\delta j}\,\mathrm{sat}(s_j/\Phi_j) - K_{Dj}\tilde{d}_j, \quad \tilde{d}_j = d_j - \hat{d}_j^f. \tag{23}$$

Without the observer ($\hat{d}_j^f = 0$), $\tilde{d}_j = d_j$. With the observer, $|\tilde{d}_j| \le \tilde{D}_j \ll D_j$, so a smaller $K_{\delta j}$ satisfies the reaching condition below, and chattering is reduced accordingly. In this study $K_{\delta j} = 1.2 K_{Dj}\tilde{D}_j$, with $\tilde{D}_j = 0.8\,\mathrm{m\,s^{-2}}$ for x, y, z, $6\,\mathrm{rad\,s^{-2}}$ for ϕ, θ and $2\,\mathrm{rad\,s^{-2}}$ for ψ. These bounds are checked against the logged observer errors in Section 3.4, which also shows that the roll/pitch bound is exceeded during gust and fault transients.

2.6.4 Altitude control

The altitude channel uses law (22) with $j = z$ and $g_z = 1$, which gives the virtual acceleration U_z; the collective thrust V_1 then follows from (19). No separate altitude law is needed, and the equivalent control contains no unknown fault factor.

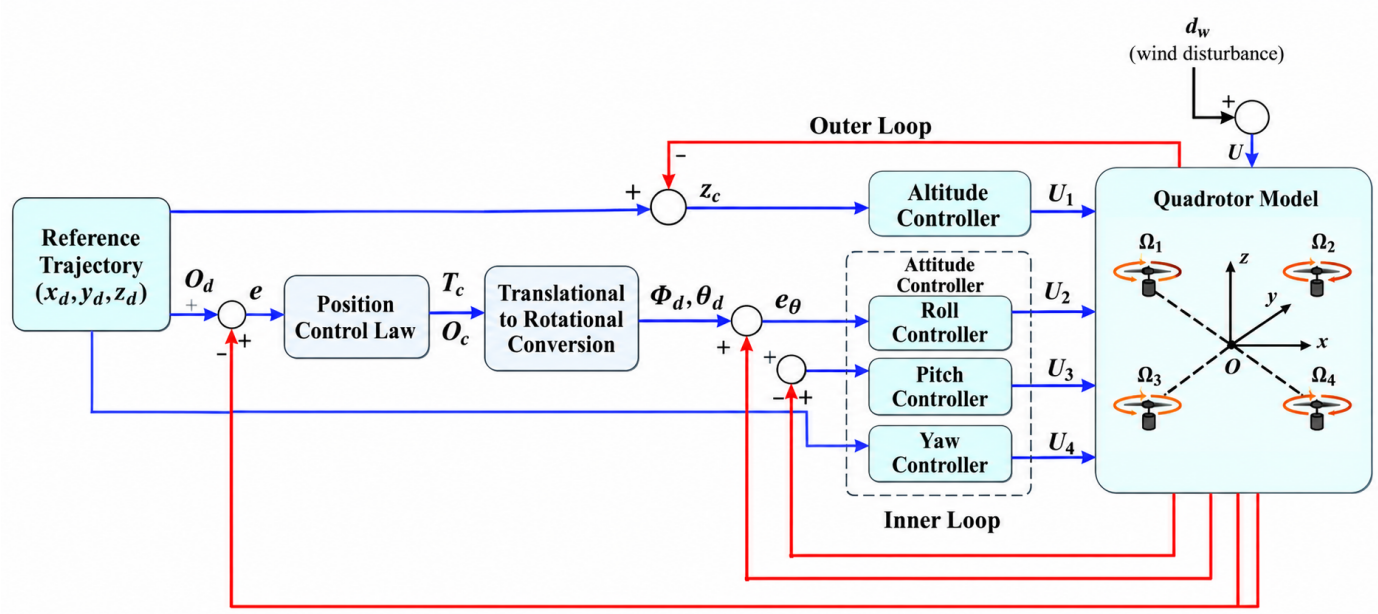


Figure 5. Control structure of the QuCo.

2.6.5 *Stability analysis*

Theorem 1 (finite-time reaching). Consider channel j of (8) under the control (22) with $\mathrm{sat}(\cdot)$ replaced by $\mathrm{sign}(\cdot)$. If $|\tilde{d}_j| \le \tilde{D}_j$ and $K_{\delta j} > K_{Dj}\tilde{D}_j$, then s_j reaches zero in a finite time

$$t_r \le \frac{1}{\beta_j}\ln\!\Big(1+\frac{\beta_j|s_j(0)|}{\chi_j}\Big), \quad \chi_j = K_{\delta j} - K_{Dj}\tilde{D}_j > 0. \tag{24}$$

Proof. Take $\mathcal{L}_{1j} = \frac{1}{2}s_j^2$. From (23),

$$\begin{aligned}\dot{\mathcal{L}}_{1j} &= -\beta_j s_j^2 - K_{\delta j}|s_j| - K_{Dj}\tilde{d}_j s_j \le -\beta_j s_j^2 - \chi_j|s_j| \\ &= -2\beta_j\mathcal{L}_{1j} - \sqrt{2}\,\chi_j\mathcal{L}_{1j}^{1/2}.\end{aligned} \tag{25}$$

The comparison lemma applied to $\frac{d}{dt}|s_j| \le -\beta_j|s_j| - \chi_j$ yields (24) [48]. ■

Theorem 2 (convergence of the auxiliary variables and the tracking error). Under the conditions of Theorem 1, consider $\mathcal{L}_j = \frac{1}{2}s_j^2 + \frac{1}{2}\varpi_j\delta_j^2$ with $\varpi_j = \beta_j\lambda_j$. Then $\mathcal{L}_j$ decays exponentially with rate at least $\kappa_j = \min(\beta_j, \lambda_j)$, so that $(s_j, \delta_j) \to 0$ exponentially with rate at least $\kappa_j/2$; $\sigma_j \to 0$ exponentially; and the tracking error $e_j \to 0$ asymptotically (Mittag-Leffler), provided that all roots of $P_j(\varsigma) = K_{Dj}\varsigma^{1+\vartheta_j} + K_{Pj}\varsigma^{\vartheta_j} + K_{Ij}$ lie in the open left half-plane of the principal Riemann sheet.

Proof. From (18), $\dot{\delta}_j = s_j - \lambda_j\delta_j$. Hence

$$\begin{aligned}\dot{\mathcal{L}}_j &= s_j\dot{s}_j + \varpi_j\delta_j(s_j - \lambda_j\delta_j) \\ &\le -\beta_j s_j^2 - \chi_j|s_j| + \varpi_j|\delta_j||s_j| - \varpi_j\lambda_j\delta_j^2.\end{aligned} \tag{26}$$

The cross term is bounded with Young's inequality, $\varpi_j|\delta_j||s_j| \le \frac{\varpi_j\lambda_j}{2}\delta_j^2 + \frac{\varpi_j}{2\lambda_j}s_j^2$. With $\varpi_j = \beta_j\lambda_j$,

$$\dot{\mathcal{L}}_j \le -\frac{\beta_j}{2}s_j^2 - \frac{\beta_j\lambda_j^2}{2}\delta_j^2 - \chi_j|s_j| \le -\kappa_j\mathcal{L}_j - \chi_j|s_j| \le 0, \tag{27}$$

so $\mathcal{L}_j(t) \le \mathcal{L}_j(0)e^{-\kappa_j t}$, and s_j, δ_j and $\dot{\delta}_j = s_j - \lambda_j\delta_j$ decay exponentially. Therefore $\sigma_j = \dot{\delta}_j + \gamma_j\delta_j \to 0$ exponentially. Finally, σ_j drives the linear fractional-order error dynamics $K_{Dj}\dot{e}_j + K_{Pj}e_j + K_{Ij}\mathcal{I}^{\vartheta_j}e_j = \sigma_j$. By Matignon's theorem [49], this system is asymptotically stable when the roots of P_j satisfy $|\arg\varsigma| > \pi/2$, and its free response decays as a Mittag-Leffler function, i.e. algebraically rather than exponentially [50]. Because the input σ_j decays exponentially, $e_j \to 0$ asymptotically. ■

Remark 1 (scope of the convergence claims). The properties above are claimed only for the signals for which they are proved: finite-time reaching of s_j (Theorem 1), exponential convergence of s_j, δ_j and σ_j, and asymptotic, not exponential or finite-time, convergence of e_j (Theorem 2). With the boundary layer, (23) is linear inside $|s_j| \le \Phi_j$. If $\chi_j > 0$, the layer is reached in finite time and s_j is ultimately bounded by $\bar{s}_j = K_{Dj}\tilde{D}_j/(\beta_j + K_{\delta j}/\Phi_j) < \Phi_j$. If the observer error temporarily exceeds the design bound so that $\chi_j \le 0$, finite-time reaching is no longer guaranteed. Outside the layer, however, the linear damping still gives $\frac{d}{dt}|s_j| \le -\beta_j|s_j| + |\chi_j|$, so s_j remains ultimately bounded by $\bar{s}_j = \max\{\Phi_j, |\chi_j|/\beta_j\}$. Consequently, δ_j, σ_j and e_j are uniformly ultimately bounded, with a residual set that shrinks with the observer error bound $\tilde{D}_j$. In the cascade (position loop feeding the

attitude loop), the attitude tracking error appears as a vanishing perturbation in d_x, d_y, d_z. Stability of the complete loop is therefore checked numerically in Section 3.4 rather than claimed globally.

Remark 2 (the reaching law of [29]). The PFOID-SMC of [29] uses $u_{j,sw} = \beta_j \delta_j + K_{\delta j}\,\mathrm{sign}(\dot{\delta}_j)$, which gives $\ddot{\delta}_j = -a_j\delta_j - \bar{b}_j\,\mathrm{sign}(\dot{\delta}_j) - K_{Dj}d_j$ with $a_j, \bar{b}_j > 0$. This is an undamped oscillator with Coulomb friction. Its natural energy function $\mathcal{L} = \frac{1}{2}a_j\delta_j^2 + \frac{1}{2}\dot{\delta}_j^2$ yields only $\dot{\mathcal{L}} \le -(\bar{b}_j - K_{Dj}D_j)|\dot{\delta}_j| \le 0$. LaSalle's principle then gives $\dot{\delta}_j \to 0$, but δ_j converges only to the set $|a_j\delta_j + K_{Dj}d_j| \le \bar{b}_j$, so σ_j and e_j need not vanish. The function $\frac{1}{2}\delta_j^2 + \frac{1}{2}\dot{\delta}_j^2$ used in [29] leaves the indefinite cross term $\delta_j\dot{\delta}_j(1 - a_j)$. The law (22) adds the linear damping $\beta_j s_j$ on $s_j = \dot{\delta}_j + \lambda_j\delta_j$, which makes the proof above possible.

2.6.6 *Genetic-algorithm tuning*

Because $J_{xx} = J_{yy}$ and the x and y channels are symmetric, the channels are grouped as $\{x, y\}$, $\{z\}$, $\{\phi, \theta\}$ and $\{\psi\}$. For each group the GA tunes $\Theta = \{K_P, K_I, K_D, \vartheta, \gamma, \beta\}$, which gives 24 decision variables. The constants λ, Φ and K_δ are fixed by the stability conditions above ($\lambda = 1$ and $\Phi = 0.2$ for the translational groups, $\lambda = 5$ and $\Phi = 0.5$ for the rotational groups). Table 1 lists the GA settings and Table 6 the bounds; gains are searched on a logarithmic scale and orders on a linear scale. The objective combines the channels explicitly and penalizes control activity:

$$\begin{aligned} J(\Theta) = &\sum_{j\in\{x,y,z,\psi\}} \int_0^{T_t} t\, e_j^2(t)\, dt \\ &+ w_{TV} \sum_k \sum_{i=1}^{4} \big|F_{i,c}[k] - F_{i,c}[k-1]\big| \\ &+ 10^4 \Big(1 + \frac{T_t - t_{div}}{T_t}\Big) \mathbb{1}_{div}. \end{aligned} \tag{28}$$

Here e_j is measured on the true state and $T_t = 30$ s. The second term, with $w_{TV} = 10^{-3}\ \mathrm{N}^{-1}$, penalizes the total variation of the commanded rotor thrusts, so the GA cannot trade chattering or noise amplification for tracking accuracy. With this weight, a total variation of 1000 N over the tuning run costs as much as one unit of ITSE. $\mathbb{1}_{div}$ is a divergence indicator, active only when the vehicle departs ($|\phi|$ or $|\theta| > 1.5$ rad) at time t_{div}. Roll and pitch are excluded from the cost because their references are generated internally by (20). Equal weights are reasonable because metres and radians have comparable magnitudes on this trajectory. Each evaluation is a full closed-loop simulation with sensors, the SMO, wind level L1 and noise, flown on a 30 s helical tuning trajectory that differs from the 300 s test trajectory. Every baseline is tuned with the same objective, scenario, population, number of generations and logarithmic bounds (Section 3.1). The GA is run ten times with different seeds for the proposed controller and three times for each baseline, and the best run is retained.

3 Simulation Results

The closed loop of Figure 4 was implemented as a fixed-step, discrete-time simulator in Python (NumPy/Numba), so that every sampling rate, delay and hold is represented explicitly. The plant (12 rigid-body states and 4 rotor states) is integrated with a fourth-order Runge-Kutta scheme at 1 kHz, the observer runs at 1 kHz on held measurements, each sensor is sampled at its own rate, and all controllers run at 200 Hz with a zero-order hold. All metrics are computed from the logged signals by a single routine. The tracking performance is evaluated for $x, y, z, \phi, \theta, \psi$, and parametric uncertainty is included to assess robustness. Table 2 gives the simulation parameters and Table 3 the GA-tuned controller parameters.

Table 2. Simulation parameters [20].

Symbol	Parameter	Value
m	Mass	1.12 kg
g	Gravitational acceleration	9.8 m/s^2
l	Arm length	0.23 m
J_{xx}	Inertia about x	0.0119 kg·m^2
J_{yy}	Inertia about y	0.0119 kg·m^2
J_{zz}	Inertia about z	0.0223 kg·m^2
b	Lift coefficient	7.73213×10^{-6} N·s^2
J_r	Rotor inertia	8.5×10^{-4} kg·m^2
K_f	Aerodynamic force constant	3.13×10^{-5} N·s^2
k_m	Aerodynamic moment constant	7.5×10^{-7} N·m·s^2
K_t	Translational drag constant	diag(0.1, 0.1, 0.15) N·s/m
K_r	Rotational drag constant	diag(0.1, 0.1, 0.15) N·m·s
τ_m	Rotor time constant	0.02 s
$F_{\max}$	Maximum thrust per rotor	6 N (2.2× hover)

3.1 Simulation set-up

Table 4 lists the on-board sensor models used in the loop.

Table 3. GA-tuned parameters of the proposed controller: best run, with mean ± standard deviation over the ten GA runs in parentheses.

Group	K_P	K_I	K_D	ϑ	γ	β	λ (fixed)	Φ (fixed)	$K_\delta = 1.2K_D\tilde{D}$
$\{x, y\}$	0.175 (0.26 ± 0.14)	1.111 (1.80 ± 0.76)	0.541 (0.87 ± 0.34)	0.948 (0.90 ± 0.04)	2.653 (3.02 ± 1.16)	6.516 (5.60 ± 1.33)	1	0.2	0.519
$\{z\}$	3.559 (5.23 ± 3.32)	0.016 (0.06 ± 0.04)	1.958 (1.52 ± 0.62)	0.336 (0.38 ± 0.21)	4.132 (4.86 ± 3.81)	2.588 (2.51 ± 4.00)	1	0.2	1.879
$\{\phi, \theta\}$	1.390 (0.59 ± 0.56)	9.068 (6.84 ± 3.32)	0.257 (0.31 ± 0.10)	0.849 (0.62 ± 0.18)	3.575 (8.82 ± 6.39)	0.579 (3.91 ± 4.37)	5	0.5	1.854
$\{\psi\}$	1.835 (5.46 ± 7.93)	0.265 (1.18 ± 1.68)	0.271 (1.17 ± 0.70)	0.417 (0.60 ± 0.17)	4.737 (5.96 ± 4.67)	6.207 (3.14 ± 1.67)	5	0.5	0.650

Table 4. On-board sensor models used in the loop (Eq. (11)).

Sensor	Measured quantity	Rate	Bias	Noise (1σ)
Gyroscope (MEMS IMU)	body rates p, q, r	200 Hz	$(0.010, -0.012, 0.008)$ rad/s + random walk 10^{-4} rad s$^{-1}/\sqrt{\text{s}}$	0.005 rad/s
AHRS	ϕ, θ, ψ	100 Hz	$(0.005, -0.004, 0.010)$ rad	0.01 rad (ϕ, θ), 0.02 rad (ψ)
RTK-GNSS	x, y	10 Hz (via link)	$(0.02, -0.015)$ m	0.03 m
Barometer	z	50 Hz	0.04 m	0.05 m

3.1.1 *Trajectories and scenarios*

The test trajectory is a 300 s figure-of-eight with simultaneous altitude and heading changes, $x_d = 4\sin(2\pi t/60)$, $y_d = 3\sin(4\pi t/60)$, $z_d = 2.5 + \sin(2\pi t/100)$ and $\psi_d = (\pi/6)\sin(2\pi t/120)$. The vehicle starts in hover at the first set-point. The GA uses a different 30 s helix, $x_d = 2\sin(2\pi t/20)$, $y_d = 2[1 - \cos(2\pi t/20)]$, $z_d = 1 + 0.05t$ and $\psi_d = 0.3\sin(2\pi t/15)$, so every test result is obtained on a trajectory the GA never saw. Table 5 defines the scenario matrix. Every controller is flown in every scenario on the same trajectory over the same window, with five independent realizations (seeds) of sensor noise, turbulence, jitter and packet loss.

3.1.2 *Baselines and GA settings*

Five baselines receive the same sensors, the same observer state estimates and the same position/attitude cascade, thrust mapping (19)-(20) and reference feed-forward $\ddot{y}_{j,d}$. They differ only in the control law and do not use $\hat{d}_j$, which is part of the proposed design.

- PID: $u_j = g_j^{-1}\big(\ddot{y}_{j,d} + K_P e_j + K_I \int e_j\,dt + K_D \dot{e}_j\big)$.
- Conventional SMC: $s_j = \dot{e}_j + c_j e_j$ and $u_j = g_j^{-1}\big(\ddot{y}_{j,d} - f_j + c_j \dot{e}_j + k_j s_j + K_j\,\mathrm{sat}(s_j/0.2)\big)$.
- FOPID [52]: $u_j = g_j^{-1}\big(\ddot{y}_{j,d} + K_P e_j + K_I \mathcal{I}^{\alpha} e_j + K_D \mathcal{D}^{\mu} e_j\big)$.
- Super-twisting SMC (STSMC) [26, 53]: $u_j = g_j^{-1}\big(\ddot{y}_{j,d} - f_j + c_j \dot{e}_j + k_1 |s_j|^{1/2}\,\mathrm{sign}(s_j) + k_2 \int \mathrm{sign}(s_j)\,dt\big)$.
- The PFOID-SMC law of [29] with the switching term $\beta_j \delta_j + K_{\delta j}\,\mathrm{sign}(\dot{\delta}_j)$ (Remark 2), normalized by $g_j K_{Dj}$ so that the gains are dimensionally consistent in all channels.

All laws use the same four channel groups and are tuned by the GA of Table 1 with objective (28), the same tuning scenario and the bounds of Table 6. The law of [29] is also evaluated with its originally reported gains.

3.1.3 *Performance metrics*

All metrics are computed by one routine from signals logged at the 200 Hz control rate over the same window $[0, T]$, with $T = 300$ s and $N = T/T_s$ samples. Errors are taken between the true reference and the true state:

$$\begin{aligned} &\mathrm{RMSE}_j = \sqrt{\tfrac{1}{N}\textstyle\sum_{k=1}^{N} e_j^2[k]}, \\ &\mathrm{ISE}_j = T_s \textstyle\sum_k e_j^2[k] = T\,\mathrm{RMSE}_j^2, \\ &\mathrm{ITSE}_j = T_s \textstyle\sum_k t_k\, e_j^2[k], \quad \mathrm{IAE}_j = T_s \textstyle\sum_k |e_j[k]|. \end{aligned} \tag{29}$$

The identity $\mathrm{ISE} = T\,\mathrm{RMSE}^2$ is checked in the code for every run. The maximum error $e_{j,\max} = \max_k |e_j[k]|$ and the settling time t_s are also reported. Here t_s is the first time after which $|e_j|$ remains within 0.1 m (position) or 0.02 rad (attitude) for 10 s; in fault scenarios the same definition, measured from the fault onset, gives the recovery time. Control effort and chattering are quantified by

$$\begin{aligned} &E_u = T_s \textstyle\sum_k \sum_{i=1}^{4} F_{i,c}^2[k], \\ &TV = \textstyle\sum_k \sum_{i=1}^{4} \big|F_{i,c}[k] - F_{i,c}[k-1]\big|, \\ &E_{ind} = T_s \textstyle\sum_k \sum_{i=1}^{4} \dfrac{F_{i,c}^{3/2}[k]}{\sqrt{2\varrho A_p}}, \end{aligned} \tag{30}$$

where E_{ind} is the ideal induced (momentum-theory) rotor energy, with air density $\varrho = 1.225$ kg/m^3 and

Table 5. Scenario definitions. Wind acts through the drag term $K_t(\dot{\mathbf{p}} - \mathbf{w})$; gusts use the 1−cosine shape of [51].

Scenario	Definition
Nominal (ideal)	True states fed back; no noise, bias or disturbance
Nominal (sensors)	Sensors of Table 4 + SMO; no disturbance
Disturbance L1/L2/L3	Mean wind 2/4/6 m/s at 30°; 1−cos gusts of 3/6/9 m/s over 6 s at $t = 60$ s and 200 s; Gauss-Markov turbulence (1 s correlation) 0.5/1.0/1.5 m/s; torques $\tau_\phi = A[\sin(0.3t) + 0.5\sin(1.1t + 1)]$, $\tau_\theta = A[\cos(0.25t) + 0.5\sin(0.9t)]$, $\tau_\psi = 0.5A\sin(0.2t)$ with $A = 5/10/20$ mN·m
PU +10/+20/+30 %	Plant mass and all inertias increased by 10/20/30 % (controllers and observer use nominal values)
Fault 20/40/60 %	Step LOE of motor 1, $\rho_1 = 0.2/0.4/0.6$, at $t = 100$ s
Comm. C1/C2/C3	Delay 20/50/100 ms, jitter 10/20/40 ms, packet drop 5/10/20 %, 1 cm quantization, 20 Hz, on the reference up-link and the GNSS link
Combined (worst case)	Disturbance L2 + PU +20 % + 20 % fault at 100 s + Comm. C2
Sweeps	Sensor noise ×0.5-×4; delay 0-200 ms (no drop); drop 0-50 % (20 ms delay); all with disturbance L1

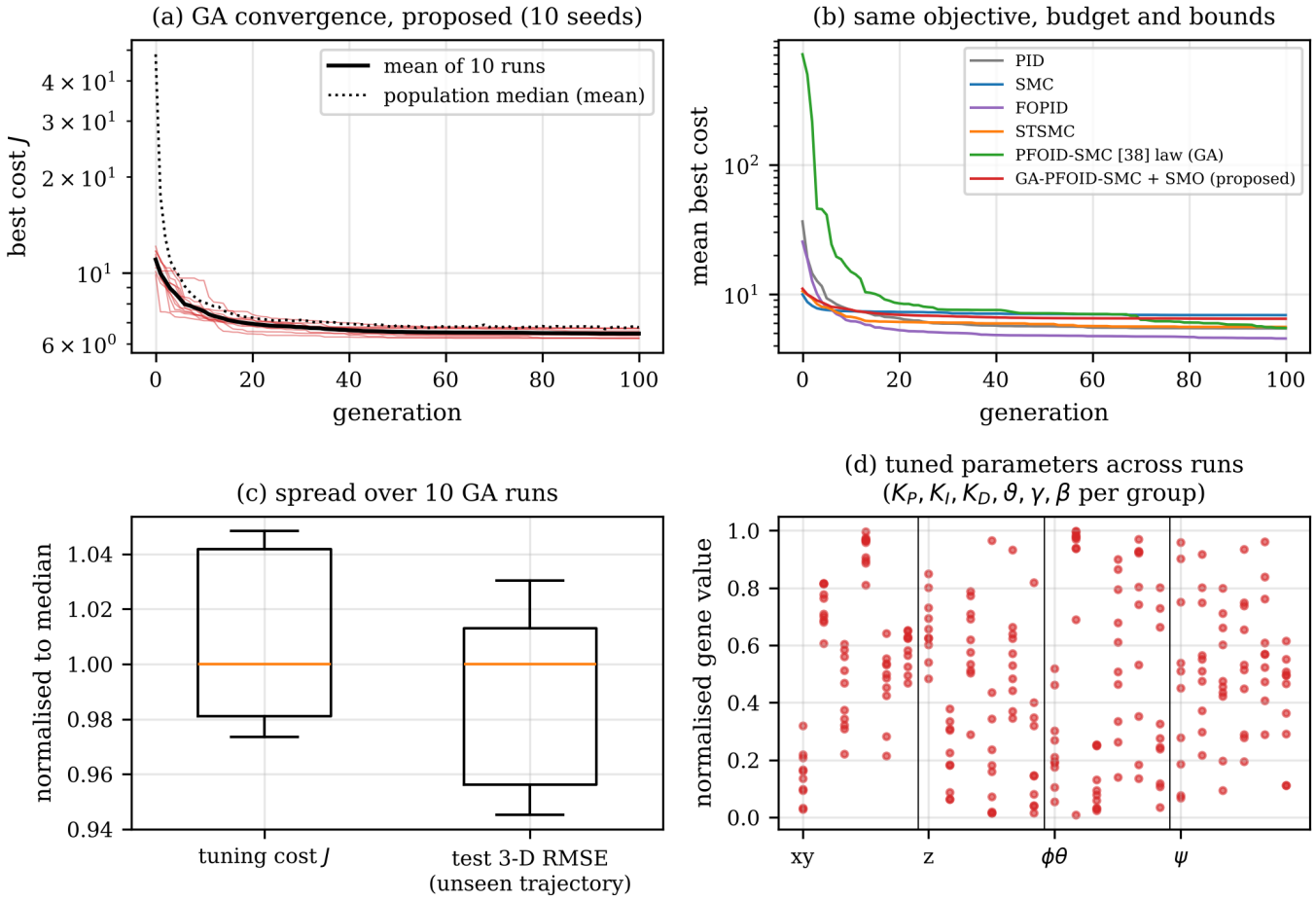


Figure 6. GA reproducibility: (a) best cost per generation for ten seeds (thin) and their mean (thick), with the mean population median; (b) mean best cost of every controller under the same objective, budget and bounds; (c) spread of the final cost and of the 3-D RMSE on the unseen test trajectory over the ten runs; (d) normalized tuned genes of the ten runs.

disc area $A_p = \pi(0.1\ \mathrm{m})^2$, used as a proxy for electrical energy. The high-frequency (HF) share is the fraction of the power spectrum of V_2 above 5 Hz. The 3-D position RMSE, $\sqrt{N^{-1}\sum(e_x^2 + e_y^2 + e_z^2)}$, is used as a single summary metric.

3.2 GA tuning and reproducibility

Figure 6 shows the convergence of the ten GA runs for the proposed controller and the mean convergence of

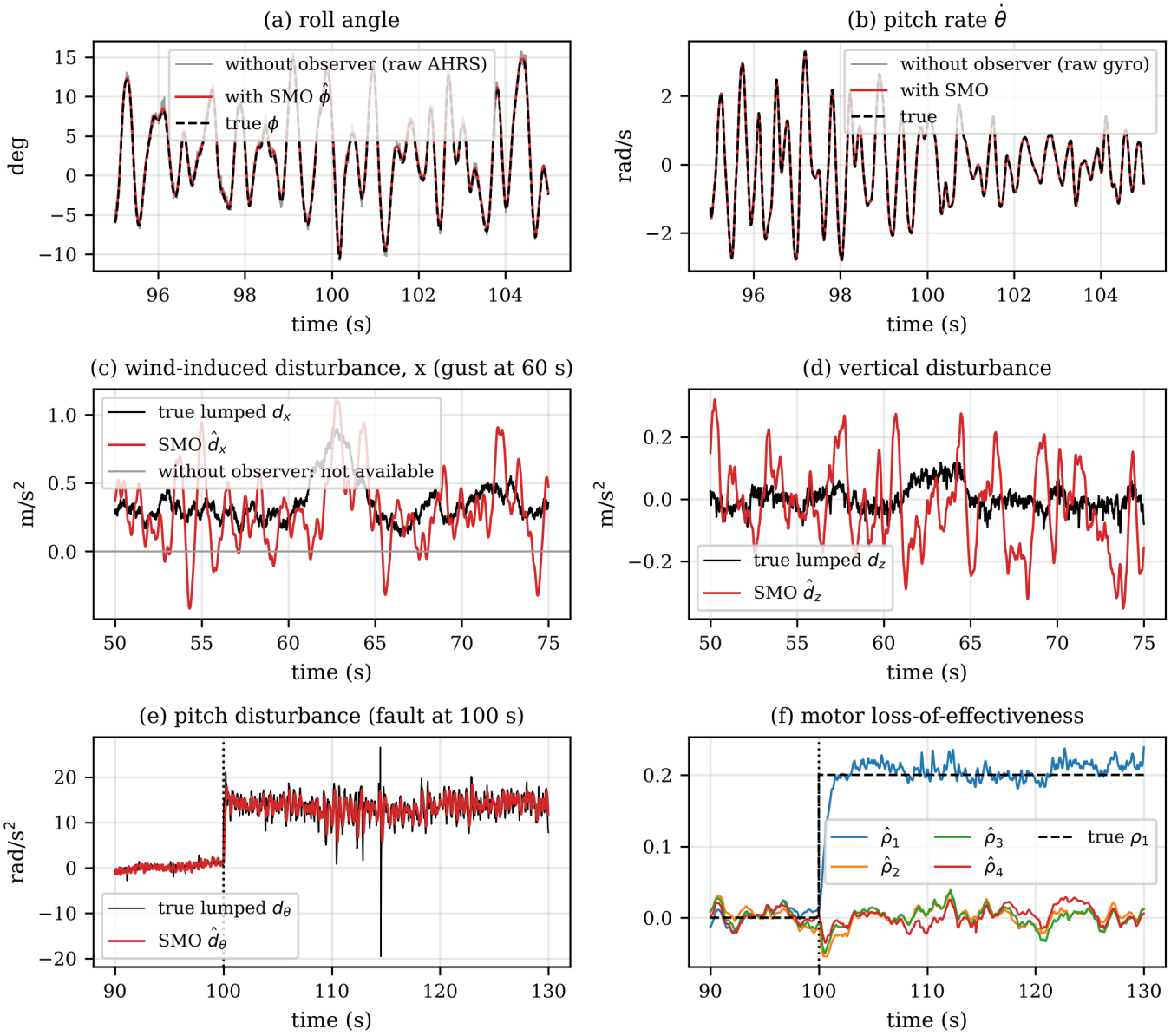


Figure 7. Estimated vs. true states with and without the observer (L2 + 20 % motor-1 fault at 100 s): (a) roll angle; (b) pitch rate; (c) wind-induced disturbance in x (gust at 60 s); (d) vertical disturbance; (e) pitch disturbance across the fault; (f) per-motor loss-of-effectiveness estimates.

every controller under the same budget, and Table 7 lists the cost statistics. The ten runs of the proposed controller ended at $J = 6.45 \pm 0.19$ (best 6.23, worst 6.70), a coefficient of variation of 2.9 %. More importantly, the ten gain sets give a 3-D RMSE of 0.124 ± 0.004 m on the 300 s test trajectory (Dist. L1; best 0.119 m, worst 0.129 m), and none of them diverged. The tuned genes are spread across the bounds (Figure 6(d)), which indicates that the cost surface is flat in several directions; this is also why some standard deviations in Table 3 are large even though the closed-loop performance is consistent. On the tuning objective itself, the GA-tuned FOPID (4.14), the law of [29] (4.53), PID (5.24) and STSMC (5.39) reached lower costs than the proposed controller (6.23). The tuning scenario is mild (wind level L1, nominal parameters), and the rest of this section shows that this ranking does not hold under stronger disturbances, uncertainty and faults. Table 8 lists the original gains of [29] and the GA-tuned baseline gains.

3.3 Sensing and the sliding mode observer

Figure 7 compares the observer estimates with the true states and with the raw measurements of the same flight (disturbance L2 with a 20 % motor-1 fault at 100 s). The SMO removes the gyroscope bias and keeps the attitude error at the level of the unobservable AHRS bias (Figure 8(a)). It reconstructs the wind-

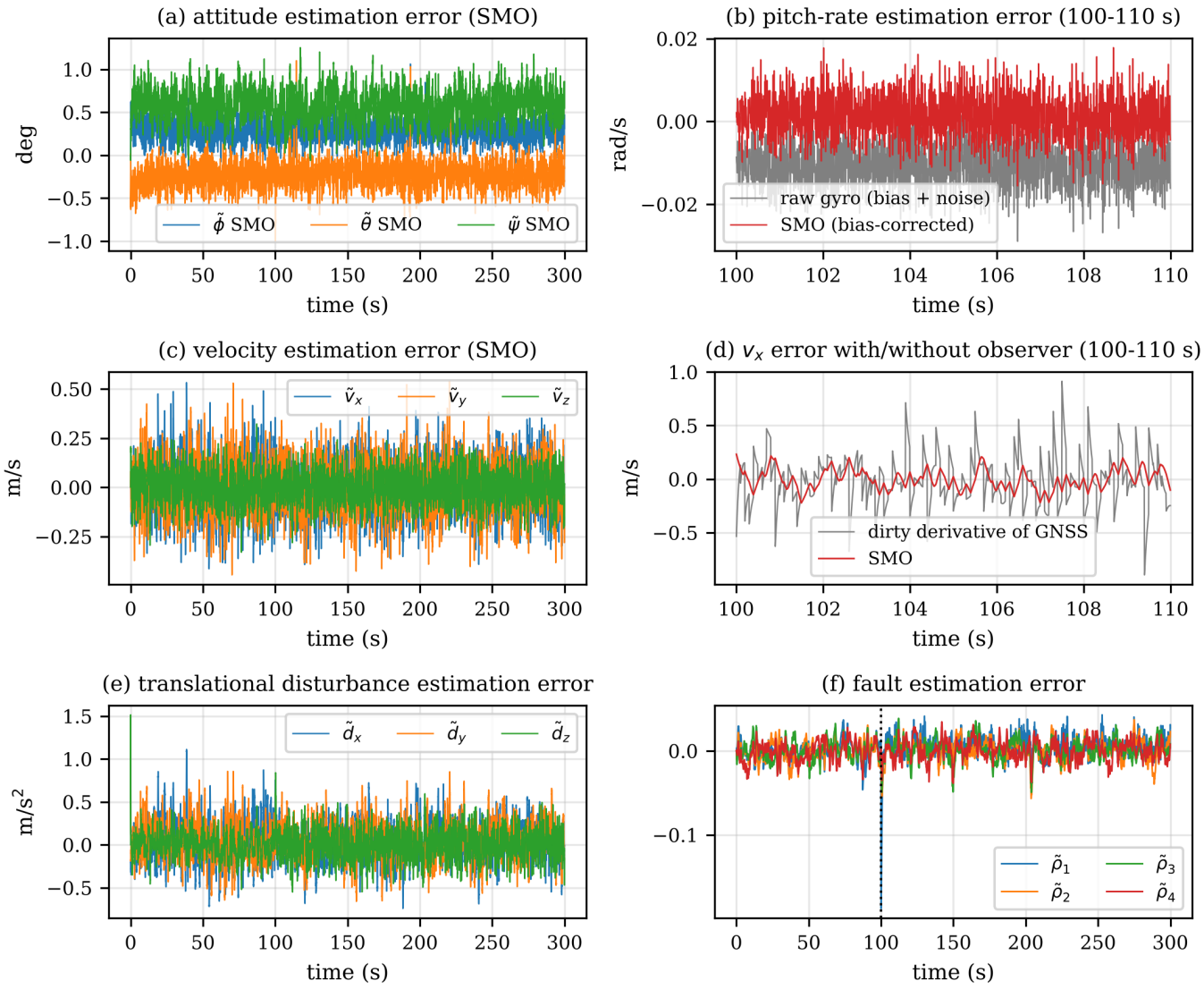


Figure 8. Estimation error vs. time for each estimated quantity: (a) attitude; (b) pitch rate, raw gyroscope vs. SMO; (c) velocities; (d) v_x by dirty derivative vs. SMO; (e) translational disturbances; (f) motor-fault estimates (fault at 100 s).

Table 6. Tuned parameters and search bounds per channel group $\{x, y\}, \{z\}, \{\phi, \theta\}, \{\psi\}$.

Controller	Tuned parameters [bounds]	Genes
PID	K_P [0.1, 30], K_I [0.01, 10], K_D [0.1, 20]	12
SMC	c [0.2, 20], k [0.1, 30], K [0.01, 10]	12
FOPID	K_P [0.1, 30], K_I [0.01, 10], K_D [0.1, 20], α [0.3, 1], μ [0.6, 1.4]	20
STSMC	c [0.2, 20], k_1 [0.1, 30], k_2 [0.1, 100]	12
PFOID-SMC law of [29]	K_P [0.1, 30], K_I [0.01, 10], K_D [0.2, 5], ϑ [0.2, 0.95], γ [0.5, 20], β [0.5, 1000], K_δ [0.01, 200]	28
Proposed	K_P [0.1, 30], K_I [0.01, 10], K_D [0.2, 5], ϑ [0.2, 0.95], γ [0.5, 20], β [0.5, 30]	24

and fault-induced lumped disturbances, including the 14 rad/s^2 pitch disturbance created by the fault, and it isolates and sizes the faulty motor: $\hat{\rho}_1$ converges to the true value 0.2 within about 1 s, while $\hat{\rho}_2$-$\hat{\rho}_4$ stay close to zero. Without the observer no disturbance or fault estimate exists, and the velocity obtained by differentiating the 10 Hz GNSS signal has more than twice the error of the SMO velocity (RMS 0.28 vs. 0.13 m/s, Figure 8(d)). Figure 8 shows the estimation errors over the whole flight.

The effect on tracking is shown in Figure 9 and in the ablation of Figure 10 and Table 9. With ideal state feedback (A1), the proposed law gives a 3-D RMSE of 0.097 m in this scenario. When the same gains are fed with the sensor signals but without the observer (A2), the loop diverged in all five seeds, between 111 s and 255 s. The noisy differentiated velocity, the uncompensated gyroscope bias and the missing disturbance feed-forward drive the attitude errors to

Table 7. GA statistics over independent runs (cost J of Eq. (28) on the tuning trajectory) and generalization of the proposed controller to the unseen test trajectory.

Controller	Genes	Runs	Mean J	Std	Best	Worst	Time per run (s)
PID	12	3	5.433	0.236	5.243	5.766	332
SMC	12	3	6.881	0.185	6.627	7.063	333
FOPID	20	3	4.544	0.322	4.140	4.929	346
STSMC	12	3	5.583	0.142	5.394	5.736	332
PFOID-SMC law of [29]	28	3	5.476	1.250	4.528	7.243	298
Proposed	24	10	6.451	0.188	6.225	6.705	345
Proposed: test 3-D RMSE (m) of the 10 solutions	-	10	0.1240	0.0038	0.1185	0.1292	-

Table 8. Original gains of the PFOID-SMC of [29] and GA-tuned gains of the baselines, per channel group.

Controller	$\{x, y\}$	$\{z\}$	$\{\phi, \theta\}$	$\{\psi\}$
PFOID-SMC [29], original gains ($K_P, K_I, K_D, \gamma, \beta, K_\delta$; $\vartheta = 0.5$)	2, 1.1, 0.45/0.4, 2, 16, 3	5, 0.6, 2.5, 2, 16, 3	6, 0.65/2.8, 2.2, 1, 18, 2.2/3	7, 1, 0.37, 3, 20, 5.1
PID (K_P, K_I, K_D)	6.24, 9.04, 5.11	2.65, 0.0245, 0.575	0.112, 0.0105, 19.2	29.9, 9.28, 0.101
SMC (c, k, K)	1.8, 4.65, 1.23	7.6, 0.458, 0.268	0.371, 11.1, 0.053	12, 0.839, 0.109
FOPID ($K_P, K_I, K_D, \alpha, \mu$)	2.38, 0.57, 2.9, 0.93, 0.704	2.09, 0.0425, 1.02, 0.631, 0.614	28.7, 8.41, 18.7, 0.316, 0.873	26.9, 8.74, 6.35, 0.337, 0.635
STSMC (c, k_1, k_2)	4.28, 0.236, 0.849	0.581, 1.04, 0.284	11.4, 6.61, 33.1	1.85, 1.49, 6.54
PFOID-SMC [29] law, GA ($K_P, K_I, K_D, \vartheta, \gamma, \beta, K_\delta$)	0.117, 4.8, 1.24, 0.549, 0.654, 0.506, 0.18	1.44, 0.0236, 2.06, 0.52, 1.9, 3.08, 0.86	16.8, 6.77, 2.24, 0.513, 0.542, 137, 4.59	6.77, 9.05, 1.14, 0.901, 0.631, 1.67, 0.114

± 0.5 rad before the vehicle departs (Figure 9). With the observer (A3), the loop is stable in every seed with a 3-D RMSE of 0.129 m, 33 % above the ideal-feedback value. Adding the communication channel C2 (A4) raises the RMSE to 0.205 m, mainly in x and y, whose position measurements travel over the link. The noise sweep of Section 3.7 shows the same trend: without the observer the loop survives only at half the nominal noise level (0.41 m), whereas with the SMO the RMSE grows smoothly from 0.081 m ($\times 0.5$) to 0.381 m ($\times 4$).

3.4 Verification of the stability analysis

Figure 11 shows the sliding variables of the z, ϕ, θ, ψ channels for a 1 m initial altitude error with ideal sensing, together with the same quantities with sensors, the observer and disturbance L2. In the ideal case, s_j and $\dot{s}_j$ reach the boundary layer within 0.3-0.8 s and then decay linearly on the logarithmic scale, i.e. exponentially. The fitted decay rate of $\mathcal{L}_z$ is 1.99 s^{-1}, above the guaranteed rate $\kappa_z = \min(\beta_z, \lambda_z) = 1\ \mathrm{s}^{-1}$ (Table 10), and $\mathcal{L}$ decreases monotonically to the numerical floor. The tracking error e_z behaves differently. After the fast transient it decays slowly and algebraically (Figure 11(d)). This is the Mittag-Leffler behaviour predicted by Theorem 2 for the fractional-order error dynamics, and it is why the error is only claimed to converge asymptotically. With sensors and disturbances, $\mathcal{L}$ stays in a bounded band of 10^{-3}-10^{-1}, as expected from the uniform ultimate boundedness in Remark 1. The Matignon test finds no zeros of P_j in the closed right half-plane for any group. The reaching margin computed with the design bound, $\chi_j = K_{\delta j} - K_{Dj}\tilde{D}_j$, is positive for every group, but Theorem 1 requires the bound on the actual observer error. Table 10 therefore also gives the margin evaluated with the 99.9th percentile of $|d_j - \hat{d}_j^f|$ logged in the L2 + fault run. In the z and ψ groups the measured value is below the design bound. In the x, y group it exceeds the bound by 5 %, but the 20 % margin built into $K_\delta = 1.2 K_D \tilde{D}$ absorbs this ($\chi = 0.519 - 0.541 \times 0.84 = 0.065 > 0$). In the roll and pitch group the measured value during gust and fault transients (10.16 rad/s^2) is 69 % above the design value (6 rad/s^2), and the margin becomes negative, $\chi = 1.854 - 0.257 \times 10.16 \approx -0.76$. Finite-time reaching is therefore not guaranteed for s_ϕ and s_θ in these intervals. Only the ultimate bound of Remark 1 applies, $|s_{\phi,\theta}| \le \max\{\Phi, |\chi|/\beta\} = 0.757/0.579 \approx 1.31$, and the exponential convergence of Theorem 2 is recovered only after the transient, once $|\tilde{d}_j|$ falls back below $K_{\delta j}/K_{Dj} = 7.2$ rad/s^2. Because a 99.9th percentile is not a strict supremum, the margins in Table 10

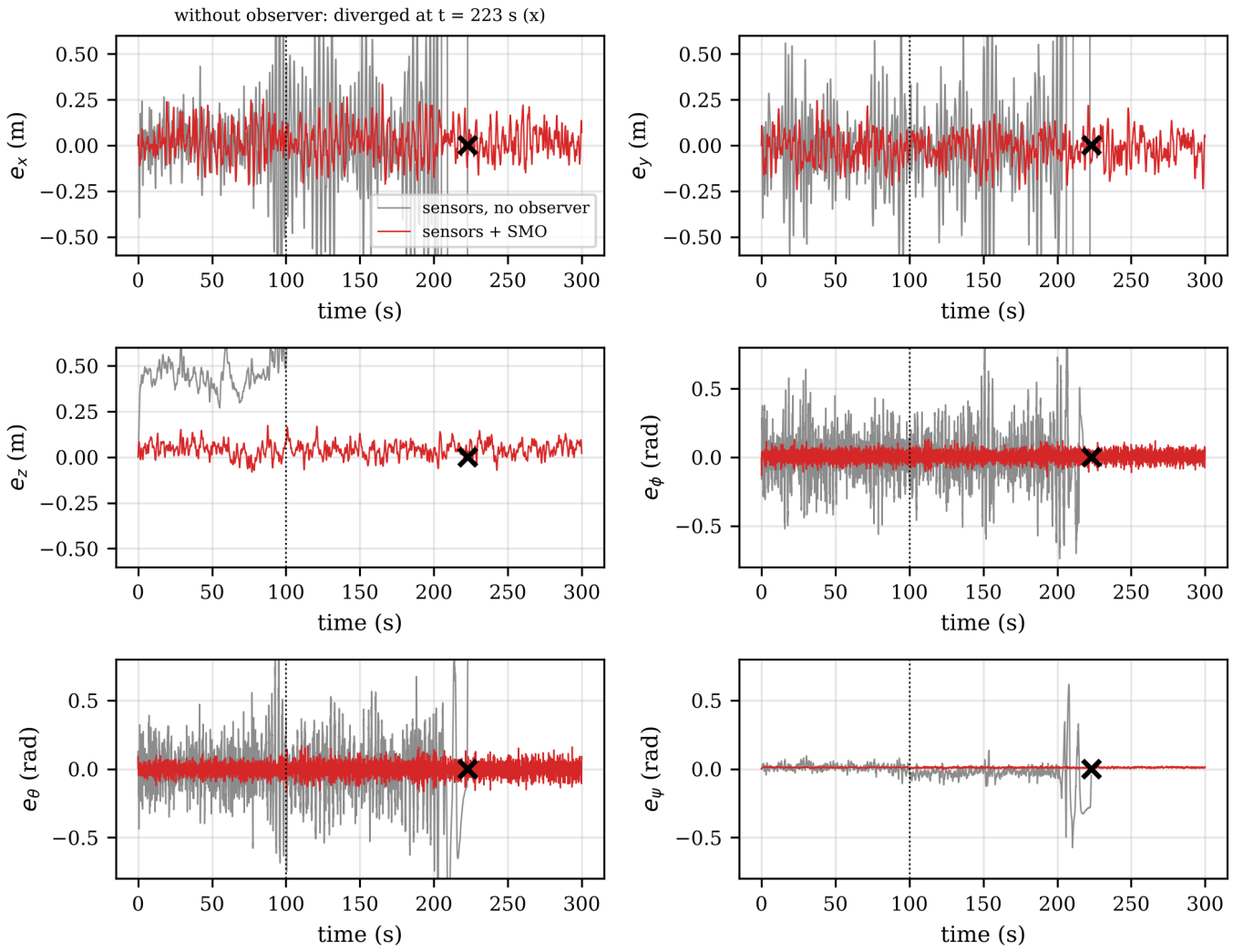


Figure 9. Tracking errors in $x, y, z, \phi, \theta, \psi$ with and without the observer (L2 + 20 % fault at 100 s, seed 1). Without the observer the loop diverged at 223 s (×).

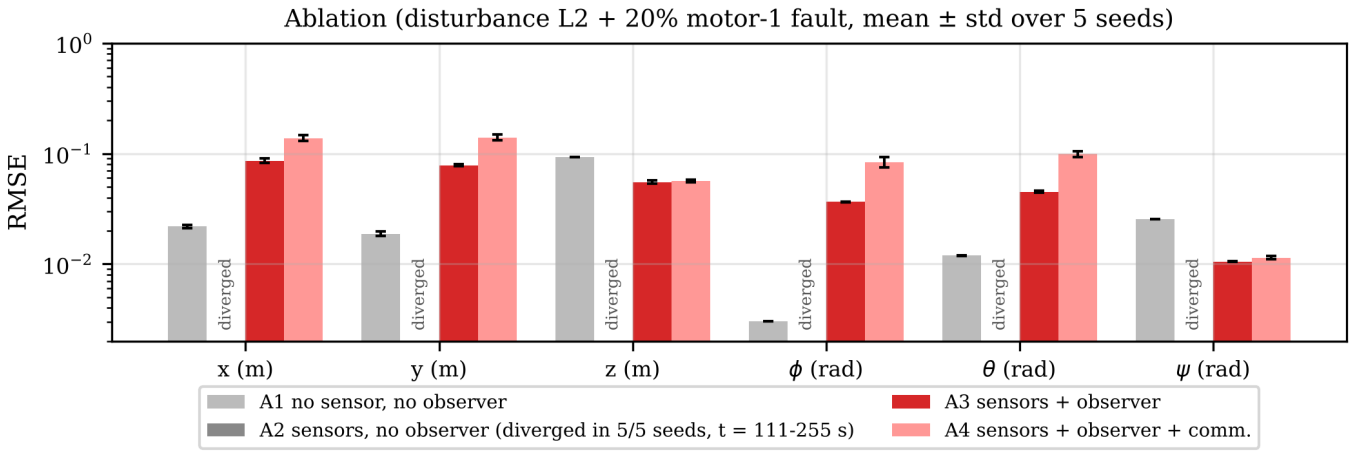


Figure 10. Ablation: RMSE of each channel for the four configurations (mean ± std over five seeds).

should be read as an empirical check, not as a proof. A switching gain designed for the observed transient error, e.g. $\bar{D}_{\phi,\theta} = 11$ rad/s^2 ($K_\delta = 1.2 \times 0.257 \times 11 \approx 3.39$), or an adaptive switching gain would restore $\chi > 0$ at the cost of more chattering.

Table 9. Ablation of the sensing, observer and communication components (proposed controller, disturbance L2 + 20 % motor-1 fault at 100 s, five seeds).

Configuration	RMSE x (m)	RMSE y (m)	RMSE z (m)	RMSE ϕ (rad)	RMSE θ (rad)	RMSE ψ (rad)	3-D RMSE (m)	TV (N)
A1 no sensor, no observer	0.0219	0.0188	0.0927	0.0030	0.0119	0.0255	0.0971	228
A2 sensors, no observer	diverged in 5/5 seeds (t = 111-255 s)							
A3 sensors + observer	0.0862	0.0785	0.0552	0.0365	0.0452	0.0105	0.1291	13 359
A4 sensors + observer + comm.	0.1379	0.1398	0.0568	0.0840	0.0991	0.0114	0.2046	15 214

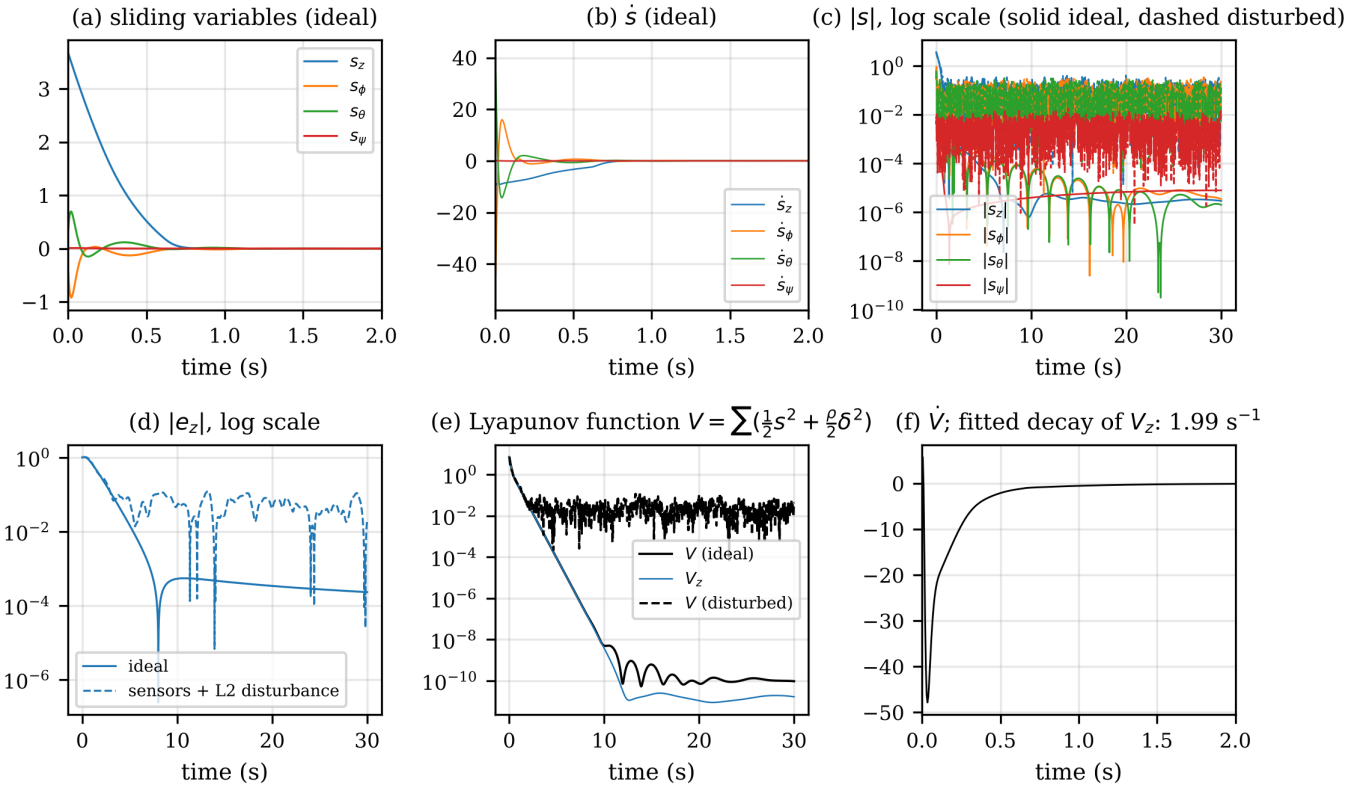


Figure 11. Stability evidence: (a) sliding variables and (b) their derivatives with ideal sensing; (c) $|s_j|$ and (d) $|e_z|$ on a logarithmic scale (solid: ideal; dashed: sensors + observer + L2); (e) Lyapunov functions $\mathcal{L}$ and $\mathcal{L}_z$; (f) $\mathcal{L}$ with the fitted exponential decay rate of $\mathcal{L}_z$.

Table 10. Stability coefficients of the proposed controller (Theorems 1-2, Remark 1). Design values use the assumed bound $\tilde{D}$; measured values use the 99.9th percentile of $|d_j - \hat{d}_j^f|$ in the L2 + fault run. The ultimate bound on s follows Remark 1 with the measured $\tilde{D}$.

					Design			Measured (99.9 %)					
Group	β	λ	$\kappa = \min(\beta, \lambda)$ (s^{-1})	K_δ	$\tilde{D}$	$K_D\tilde{D}$	χ	$\tilde{D}$	$K_D\tilde{D}$	χ	t_r bound, $s_0 = 1$ (s)	Ultimate bound on $\|s\|$	Zeros of P_j in Re ≥ 0
$\{x, y\}$	6.516	1	1.000	0.519	0.8	0.433	0.087	0.84	0.454	0.065	0.67	0.050	0
$\{z\}$	2.588	1	1.000	1.879	0.8	1.566	0.313	0.58	1.136	0.743	0.86	0.095	0
$\{\phi, \theta\}$	0.579	5	0.579	1.854	6.0	1.542	0.309	10.16	2.611	−0.757	1.82†	1.31‡	0
$\{\psi\}$	6.207	5	5.000	0.650	2.0	0.542	0.108	1.37	0.371	0.279	0.66	0.049	0

†Valid only while $|\tilde{d}_j| \leq \tilde{D}$ (design); not guaranteed during the gust and fault transients. ‡ $\max\{\Phi, |\chi|/\beta\}$, since $\chi < 0$ (Remark 1).

3.5 Comparison with the baselines: nominal conditions and disturbances

Figure 12 shows the 3-D tracking of all controllers with sensors, without and with disturbance L2. Tables 11 and 12 report every metric, recomputed from the logs over the same 300 s window. In the nominal-sensor and L1/L2 cases the GA-tuned FOPID is the most accurate controller (3-D RMSE 0.071 m nominal and 0.115 m at L2). PID (0.094/0.120 m) and the proposed controller (0.119/0.126 m) follow, and STSMC (0.128/0.149 m) and SMC (0.129/0.173 m) come last. The proposed controller is therefore not the best in nominal or mildly disturbed conditions. Its ψ RMSE (0.0104 rad) equals the best value within the noise floor set by the AHRS. As the disturbance grows, however, its error grows least (Figure 13; see also Section 3.8). From the nominal case to level L3 the 3-D RMSE of the proposed

Table 11. Tracking metrics under nominal conditions with sensors and observer (mean of five seeds, window 0-300 s; RMSE in m or rad; ISE, ITSE and IAE summed over x, y, z; $e_{\max}$ over x, y, z; t_s: time after which all position errors stay within 0.1 m for 10 s).

Controller	RMSE x	RMSE y	RMSE z	RMSE ψ	ISE	ITSE	IAE	$e_{\max}$	t_s (s)
PID	0.058	0.057	0.047	0.010	2.639	389.5	39.87	0.217	22.01
SMC	0.078	0.086	0.056	0.011	5.001	748.5	53.19	0.458	97.02
FOPID	0.038	0.039	0.046	0.011	1.531	210.0	30.93	0.234	6.092
STSMC	0.082	0.081	0.055	0.010	4.940	734.4	52.02	0.294	89.71
PFOID-SMC law of [29]	diverged in 5/5 seeds								
Proposed	0.079	0.072	0.054	0.010	4.279	645.1	49.16	0.313	79.28

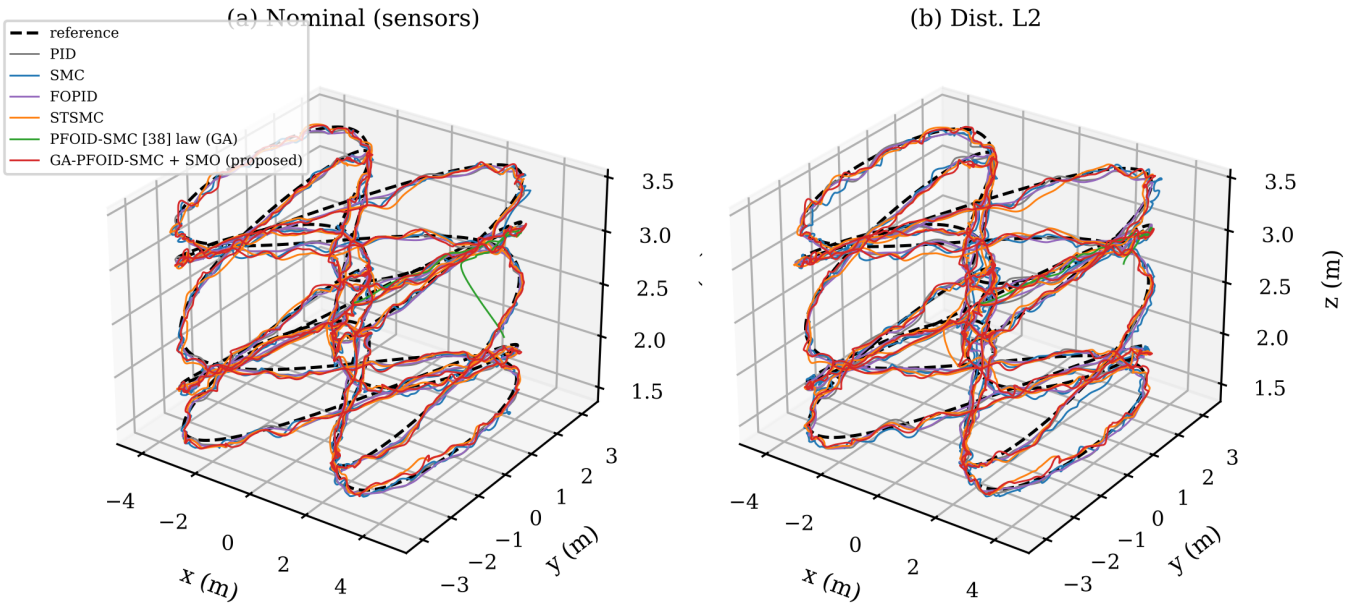


Figure 12. 3-D trajectory tracking on the 300 s test trajectory with sensors and observer: (a) no disturbance; (b) disturbance L2. The law of [29] diverged after about 15 s.

Table 12. Tracking metrics under disturbance L2 (definitions as in Table 11).

Controller	RMSE x	RMSE y	RMSE z	RMSE ψ	ISE	ITSE	IAE	$e_{\max}$	t_s (s)
PID	0.079	0.074	0.053	0.011	4.347	640.9	50.24	0.276	97.75
SMC	0.119	0.112	0.055	0.014	9.022	1416	68.87	0.581	31.86
FOPID	0.077	0.069	0.049	0.011	3.939	573.2	48.10	0.310	58.85
STSMC	0.100	0.094	0.057	0.010	6.646	983.2	59.39	0.396	95.24
PFOID-SMC law of [29]	diverged in 5/5 seeds								
Proposed	0.083	0.078	0.054	0.010	4.791	712.4	51.91	0.324	152.4

Table 13. Control effort and chattering (mean of five seeds, 300 s).

	Nominal (sensors)				Disturbance L2			
Controller	E_u (N^2·s)	TV (N)	E_{ind} (kJ)	HF (%)	E_u (N^2·s)	TV (N)	E_{ind} (kJ)	HF (%)
PID	9 214	8 619	19.87	32.60	9 232	8 757	19.89	32.53
SMC	10 719	23 499	21.52	16.18	10 508	22 127	21.30	16.53
FOPID	9 142	9 905	19.77	54.84	9 156	9 944	19.79	54.76
STSMC	9 245	8 230	19.90	17.98	9 253	8 173	19.91	18.01
PFOID-SMC law of [29]	diverged							
Proposed	9 647	13 543	20.35	14.18	9 660	13 586	20.37	14.24

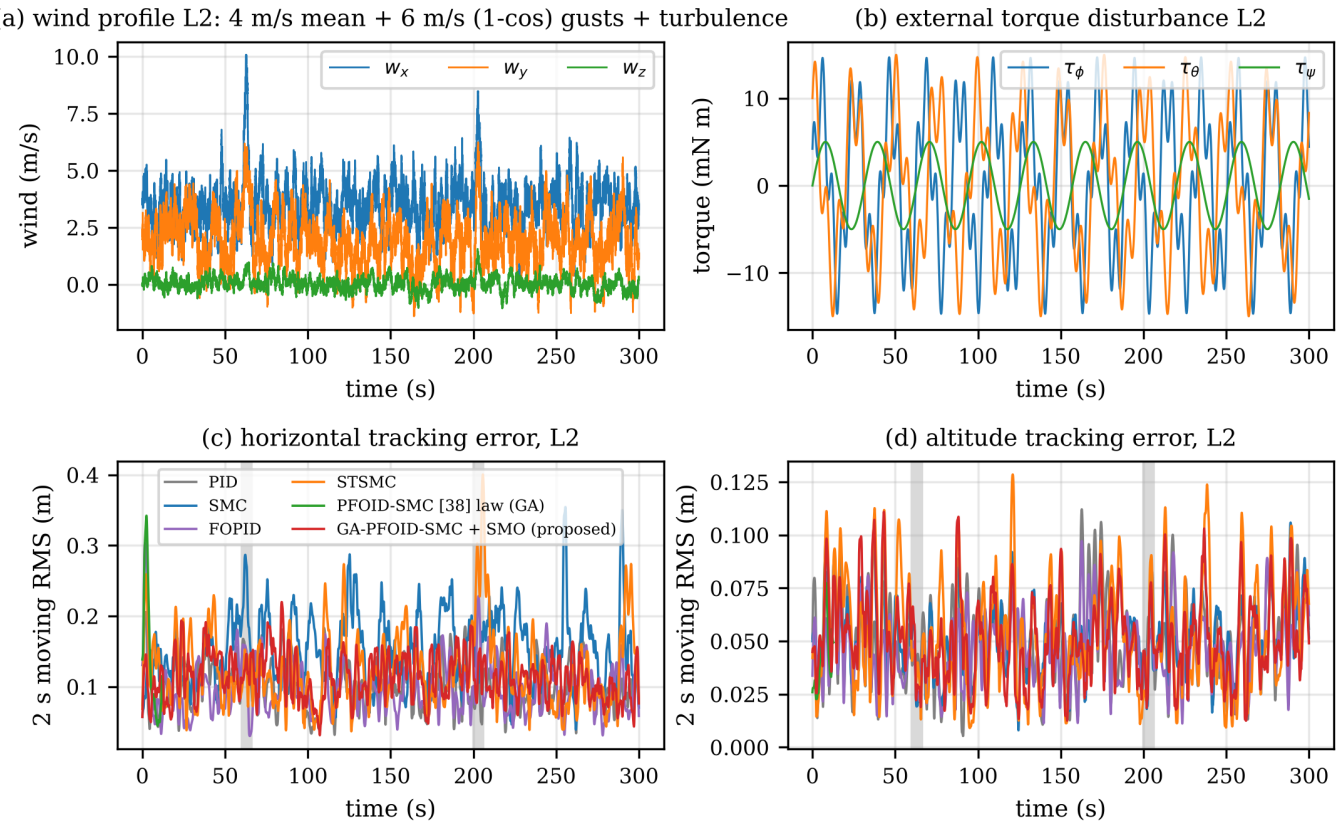


Figure 13. Disturbance L2: (a) wind profile (mean, 1−cos gusts at 60 s and 200 s, turbulence); (b) external torques; (c) horizontal and (d) altitude tracking error of all controllers as a 2 s moving RMS (shaded: gusts).

Table 14. 3-D position RMSE (m, mean ± std over five seeds) of every controller in every scenario; best in bold. "fail $(n/5)$": diverged or lost in n seeds.

Scenario	PID	SMC	FOPID	STSMC	PFOID-SMC law of [29]	Proposed
Nominal (ideal)	0.012 ± 0.000	**0.010 ± 0.000**	0.020 ± 0.000	0.011 ± 0.000	0.022 ± 0.000	**0.010 ± 0.000**
Nominal (sensors)	0.094 ± 0.001	0.129 ± 0.003	**0.071 ± 0.001**	0.128 ± 0.007	fail (5/5)	0.119 ± 0.004
Dist. L1	0.102 ± 0.002	0.137 ± 0.003	**0.084 ± 0.000**	0.136 ± 0.005	fail (5/5)	0.121 ± 0.003
Dist. L2	0.120 ± 0.002	0.173 ± 0.014	**0.115 ± 0.001**	0.149 ± 0.002	fail (5/5)	0.126 ± 0.004
Dist. L3	0.224 ± 0.054	0.294 ± 0.020	0.177 ± 0.003	0.176 ± 0.010	fail (5/5)	**0.134 ± 0.005**
PU +10 %	0.378 ± 0.001	0.278 ± 0.005	0.399 ± 0.001	0.162 ± 0.009	fail (5/5)	**0.124 ± 0.005**
PU +20 %	0.742 ± 0.001	0.545 ± 0.006	0.749 ± 0.000	0.360 ± 0.015	fail (5/5)	**0.140 ± 0.005**
PU +30 %	1.112 ± 0.001	0.823 ± 0.006	1.101 ± 0.000	0.856 ± 0.012	fail (5/5)	**0.179 ± 0.008**
Fault 20 %	fail (5/5)	fail (5/5)	0.265 ± 0.000	0.139 ± 0.005	fail (5/5)	**0.119 ± 0.004**
Fault 40 %	fail (5/5)	fail (5/5)	fail (5/5)	0.254 ± 0.012	fail (5/5)	**0.147 ± 0.007**
Fault 60 %	fail (5/5)	fail (5/5)	fail (5/5)	fail (5/5)	fail (5/5)	fail (5/5)
Comm. C1	0.130 ± 0.003	0.255 ± 0.075	**0.083 ± 0.002**	0.179 ± 0.011	fail (5/5)	0.165 ± 0.004
Comm. C2	0.155 ± 0.003	0.353 ± 0.029	**0.106 ± 0.004**	0.207 ± 0.013	fail (5/5)	0.181 ± 0.009
Comm. C3	0.229 ± 0.012	fail (1/5)	**0.205 ± 0.017**	0.320 ± 0.033	fail (5/5)	0.264 ± 0.006
Combined	fail (5/5)	fail (5/5)	0.967 ± 0.005	**0.411 ± 0.017**	fail (5/5)	fail (5/5)

controller increases by about 13 % (0.119→0.134 m), compared with 149 % for FOPID (0.071→0.177 m), 138 % for PID and 37 % for STSMC. At level L3 the proposed controller is the most accurate of all (0.134 m vs. 0.176 m for the next best). Its settling time under L2 (152.4 s, Table 12) is the longest of all controllers, because the gusts at 60 s and 200 s repeatedly push the position error out of the 0.1 m band; t_s should therefore be read together with the RMSE values.

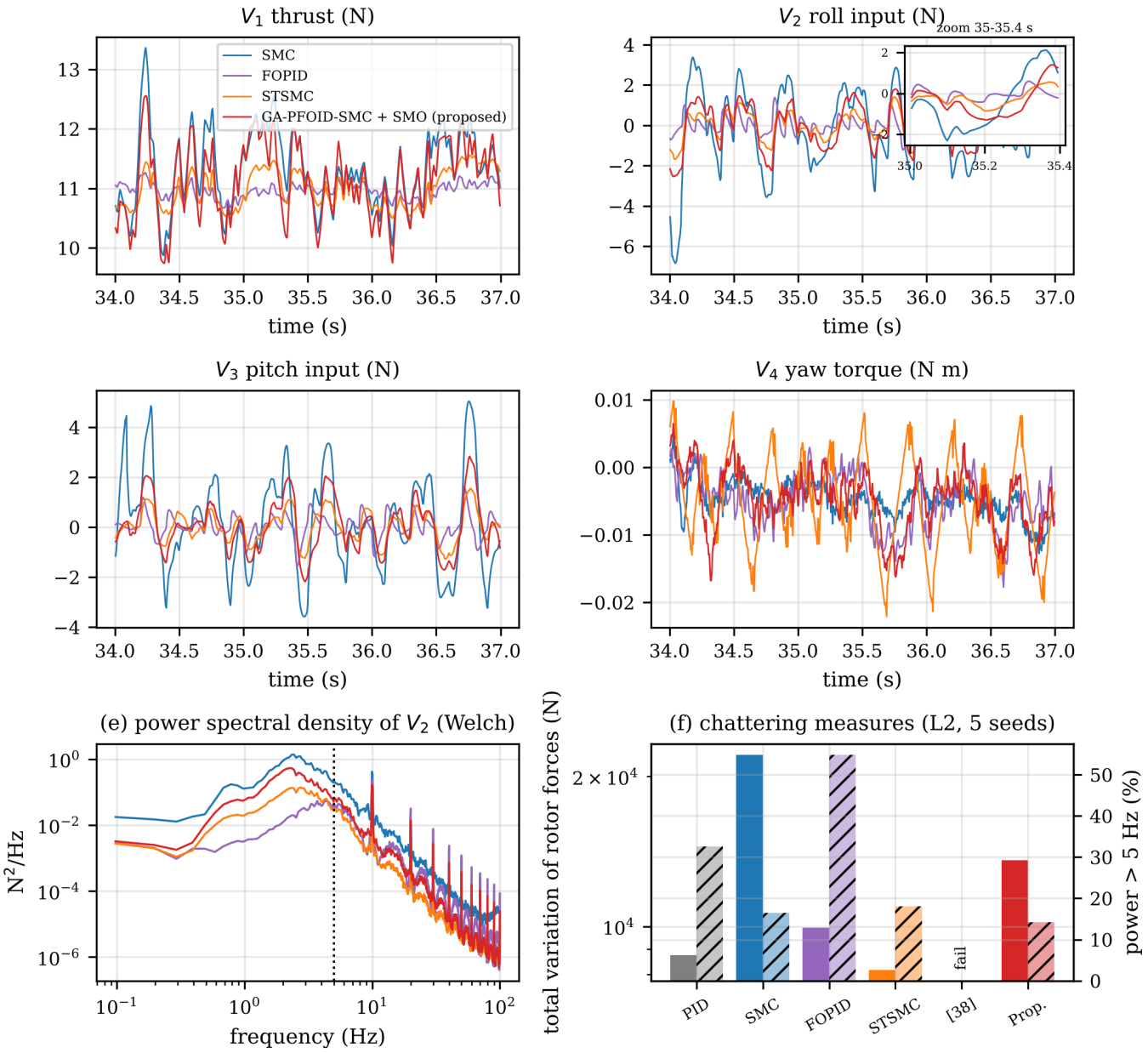


Figure 14. Control inputs under disturbance L2: (a)-(d) histories of V_1-V_4 with a zoomed inset of V_2; (e) power spectral density of V_2; (f) chattering measures: total variation of the rotor thrusts (solid) and share of V_2 power above 5 Hz (hatched), five seeds.

The control-effort measures (Table 13, Figures 14 and 15) give a mixed picture. The induced-power energy is almost the same for PID, FOPID and STSMC (19.8-19.9 kJ over 300 s). Relative to PID, the proposed controller needs 2.4 % more (20.4 kJ) and SMC 8.3 % more (21.5 kJ) in the nominal case. The proposed controller has the lowest high-frequency share of the roll input (14 % of the power above 5 Hz, against 18 % for STSMC, 33 % for PID and 55 % for FOPID), so the smaller switching gain allowed by the observer does reduce chattering in the spectral sense. Its total variation of the rotor thrusts (13.6 kN over 300 s) is, however, higher than that of PID, FOPID and STSMC (8.2-9.9 kN), because it reacts to the disturbance estimates at low and mid frequencies. A lower ISE does not by itself imply lower energy use.

3.6 Parametric uncertainty and actuator faults

The benefit of the observer-based compensation is largest when the model is wrong. With the plant mass and inertias increased by 10/20/30 %, the proposed controller keeps a 3-D RMSE of 0.124/0.140/0.179 m. The best baseline is STSMC at +10 % and +20 % (0.162/0.360 m) and SMC at +30 % (0.823 m, STSMC 0.856 m), while PID, SMC and FOPID exceed 0.5 m already at +20 % (Section 3.8). The reason can be

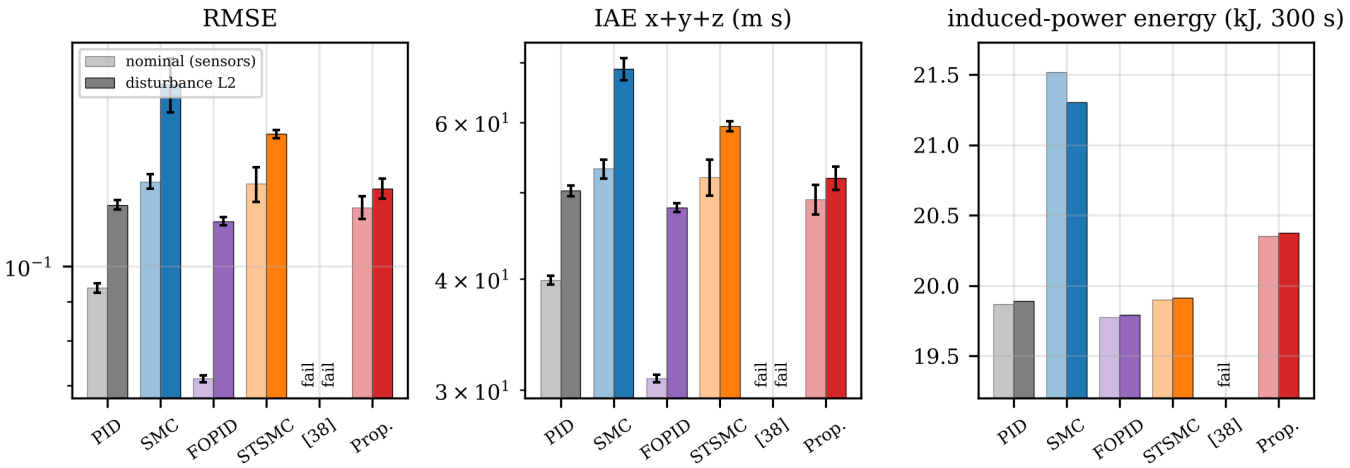


Figure 15. Summary metrics for all controllers (nominal: light; L2: dark): 3-D RMSE, summed IAE and induced-power energy (five seeds).

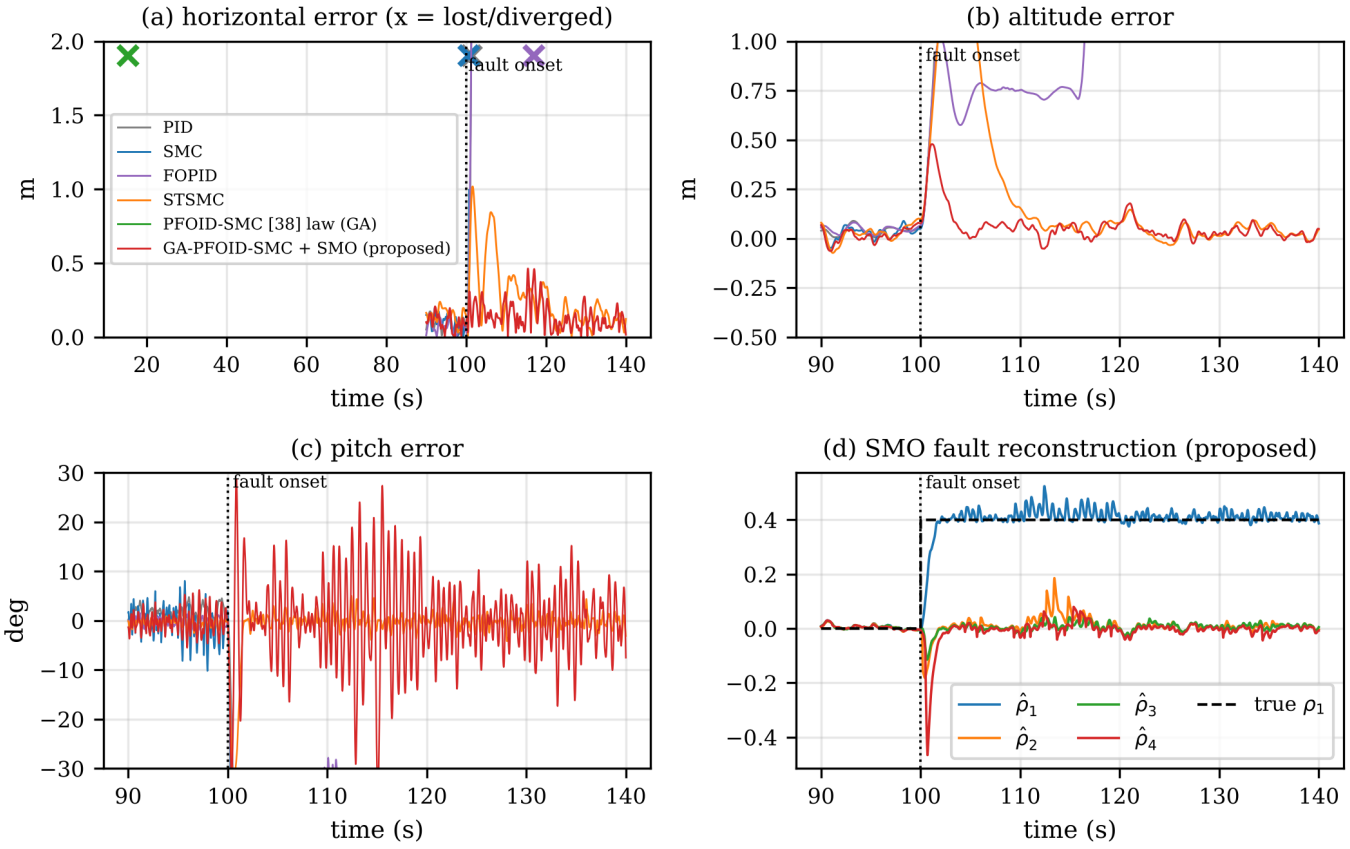


Figure 16. Actuator fault (motor 1 loses 40 % effectiveness at $t = 100$ s, dotted line): (a) horizontal, (b) altitude and (c) pitch errors of all controllers ($\times$ = lost or diverged); (d) SMO reconstruction of the per-motor loss of effectiveness.

seen in (23): the uncertainty enters d_j, which $\hat{d}_j^f$ cancels, whereas the GA-tuned baselines have very small integral gains in some channels (Table 8) and accumulate steady-state errors.

For the motor-1 loss of effectiveness at 100 s (Figure 16), PID and SMC lost the vehicle in every seed already at 20 %. FOPID survived 20 % (0.265 m) but not 40 %. The proposed controller (0.119 and 0.147 m) and STSMC (0.139 and 0.254 m) survived both. After the fault, the position errors of the proposed controller returned to the 0.1 m band 27.5 s (20 %) and 72 s (40 %) after onset, against 61 s and 101 s for STSMC. The fault is isolated and sized by $\hat{\rho}_1$ within about 1 s (Figure 16(d)). No controller tolerated a 60 %

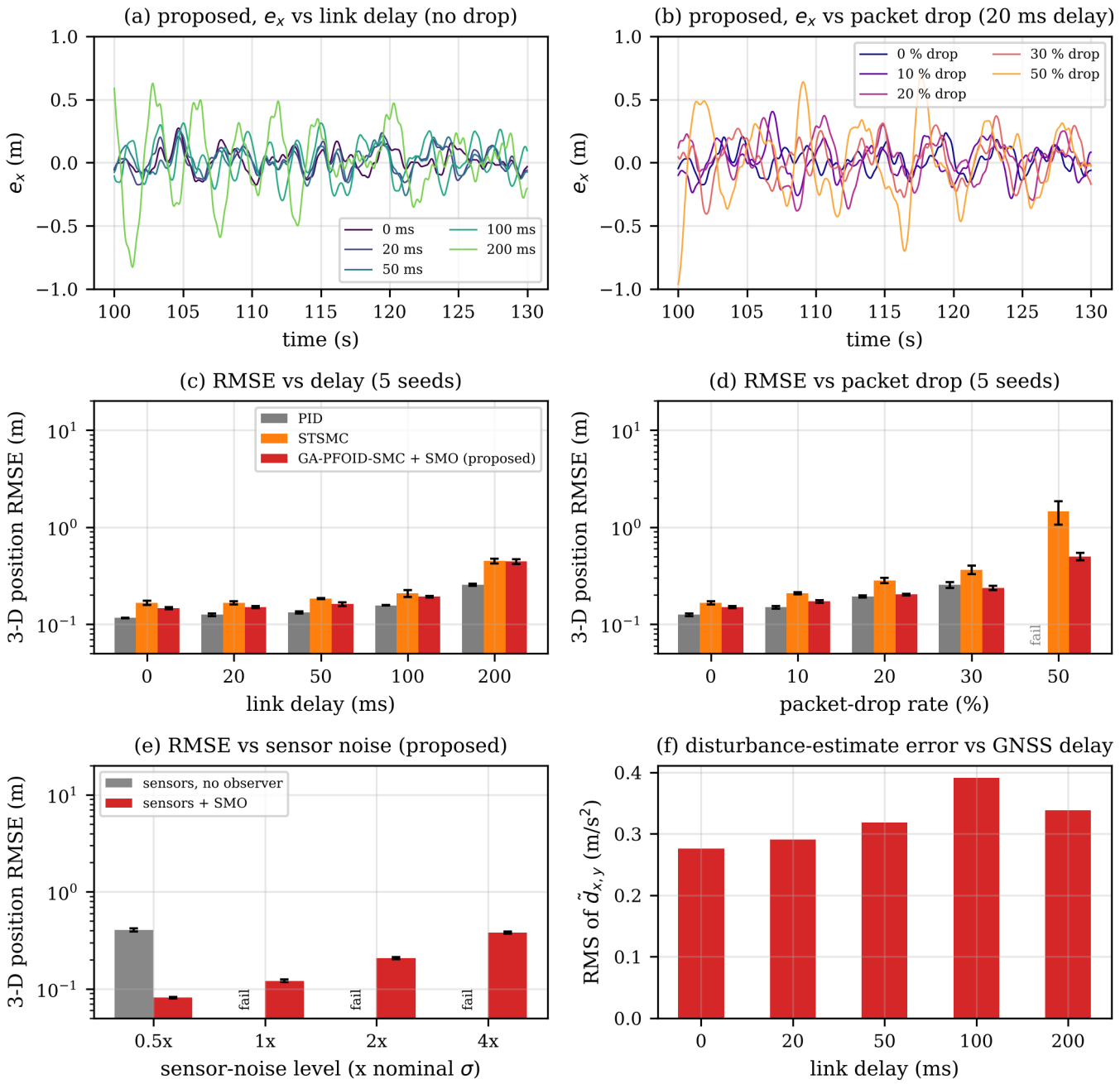


Figure 17. Communication effects on the proposed controller: (a) e_x for link delays of 0-200 ms and (b) for packet-drop rates of 0-50 %; (c) 3-D RMSE vs. delay and (d) vs. drop for PID, STSMC and the proposed controller; (e) 3-D RMSE vs. sensor-noise level with and without the observer; (f) RMS error of the translational disturbance estimate vs. GNSS delay (five seeds; "fail" = divergence in at least one seed).

loss: the faulty rotor saturates at $F_{\max}$, the remaining control authority is insufficient, and no feedback law can recover the vehicle without reconfiguring the allocation.

3.7 Communication effects

Figure 17 shows the effect of the link. With the time-stamped set-point prediction and the forward-predicted GNSS innovation (Sections 2.4 and 2.5.2), the proposed controller remains stable up to 200 ms delay (3-D RMSE 0.147, 0.151, 0.162, 0.193 and 0.443 m for 0, 20, 50, 100 and 200 ms) and up to 50 % packet drop (0.151→0.502 m). PID fails at 50 % drop, and STSMC degrades to 1.45 m. The remaining sensitivity comes from the observer: a delayed or missing GNSS sample corrupts the translational disturbance estimate, whose RMS error grows from 0.28 m/s^2 without delay to 0.39 m/s^2 at 100 ms (Figure 17(f)). In the scenario matrix (Comm. C1-C3), FOPID is the most delay-tolerant controller,

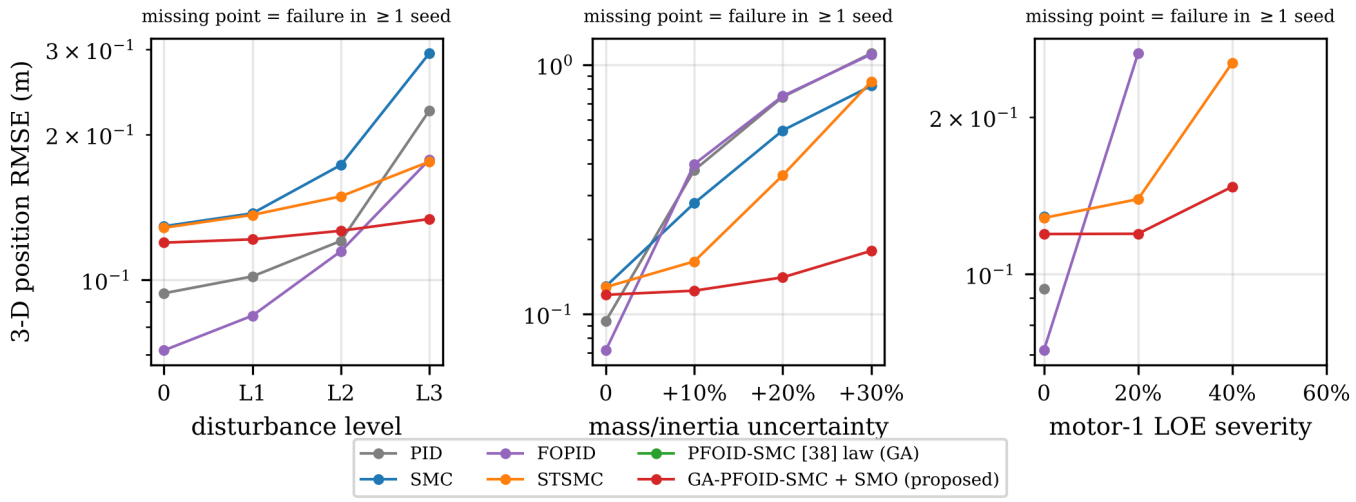


Figure 18. 3-D position RMSE vs. (a) disturbance level, (b) parametric uncertainty and (c) actuator-fault severity (mean of five seeds; a missing point is a failure in at least one seed).

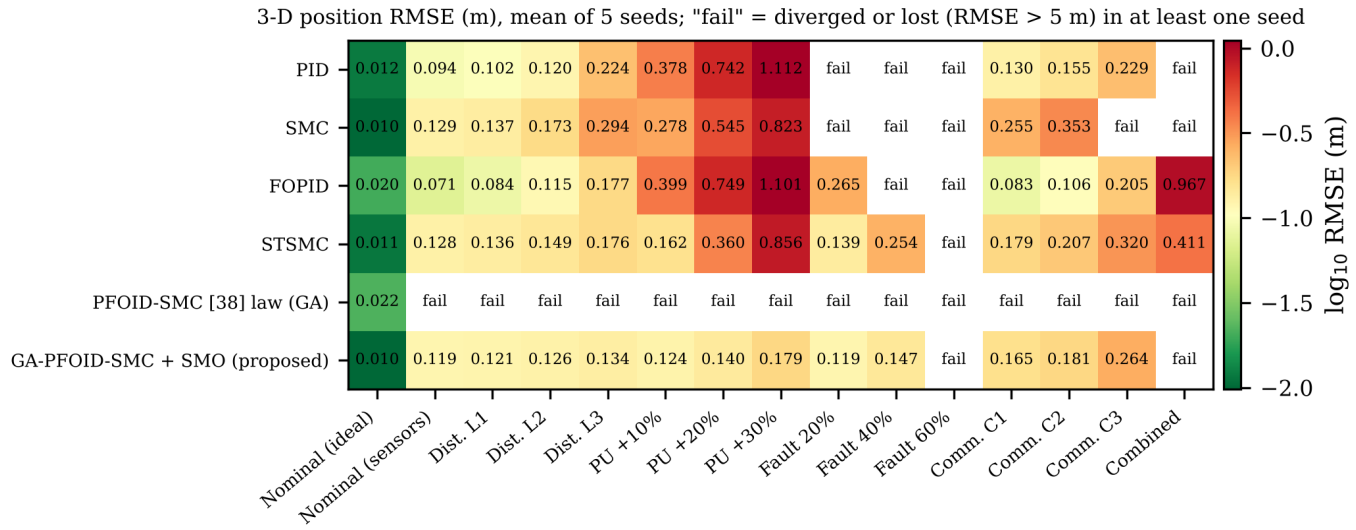


Figure 19. Heat-map of the 3-D position RMSE (m) of every controller in every scenario (mean of five seeds).

and the proposed controller ranks third behind FOPID and PID (C2: 0.106, 0.155 and 0.181 m).

3.8 Scenario matrix

Figure 18 plots the 3-D RMSE against the disturbance, uncertainty and fault levels, and Figure 19 and Table 14 summarize all 15 scenarios. The proposed controller is the most accurate in 7 of the 15 scenarios (ideal nominal, tied with SMC; L3; the three PU levels; and the 20 % and 40 % faults). FOPID is the most accurate in the nominal-sensor, L1, L2 and communication scenarios. In the combined worst case (L2 + PU +20 % + 20 % fault + C2), only STSMC (0.411 m) and FOPID (0.967 m) survive, and STSMC is the more accurate. The proposed controller failed in that case. During the 6 m/s gust at 200 s, the faulty rotor of the 20 % heavier vehicle saturated at $F_{\max}$ and the attitude could not be held. In that situation the observer feed-forward demands more thrust than the smoother STSMC, and an anti-windup or saturation-aware allocation would be needed to use the remaining margin. This limitation is discussed below.

3.9 Comparison with the PFOID-SMC of [29]

Figure 20 compares the reaching law of [29] with the proposed law. With its originally reported gains, the law of [29] diverged within 1.2-2.0 s in every scenario, including ideal state feedback. With the same GA budget as the proposed law, it tracked well with ideal state feedback (3-D RMSE 0.022 m vs. 0.010 m for the proposed law). With sensors in the loop it diverged after 12-16 s in every seed of every scenario.

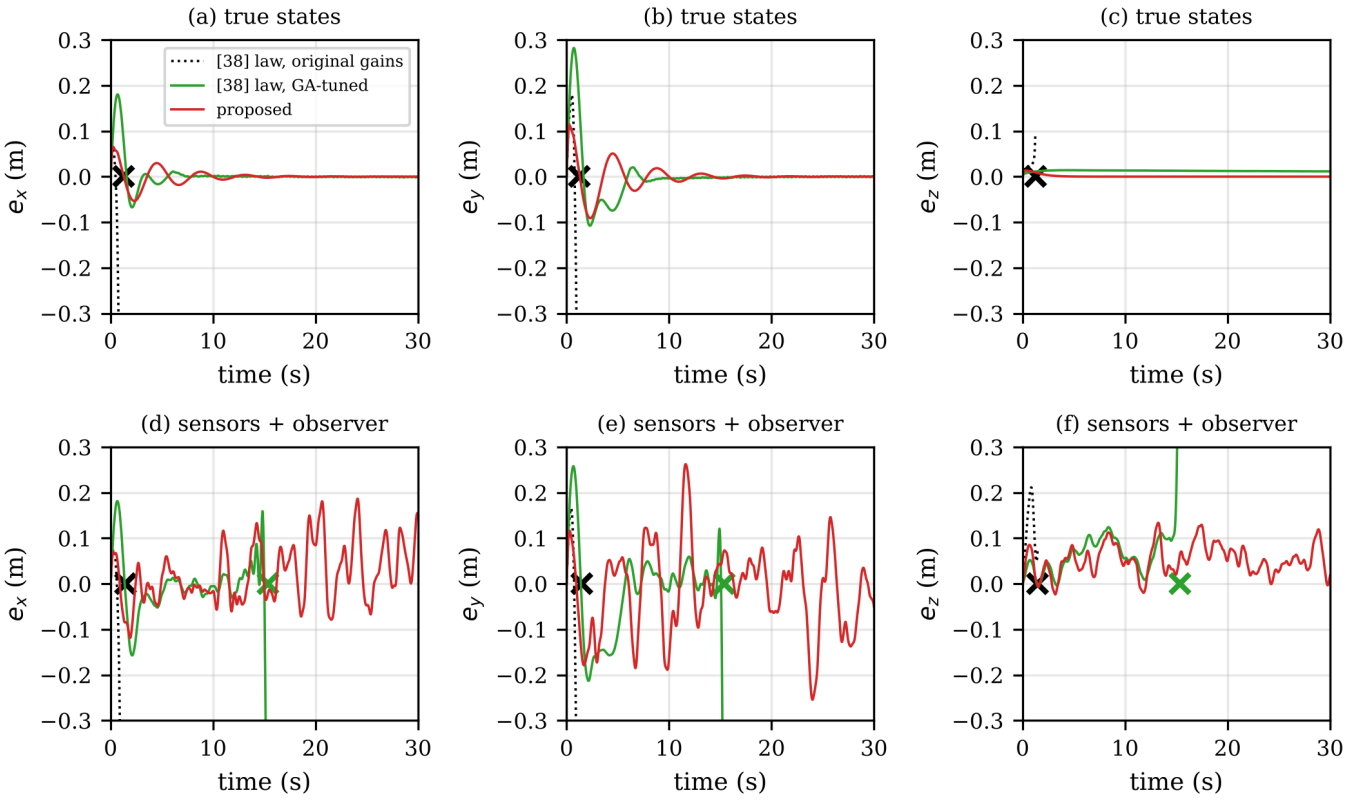


Figure 20. Reaching law of [29] (original gains: dotted; GA-tuned: green) vs. the proposed law (red), first 30 s of the test trajectory with (a)-(c) true-state feedback and (d)-(f) sensors + observer; × marks divergence.

When its 30 s tuning run was simply extended, it diverged at 31 s, so the GA had exploited a finite horizon rather than found a stabilizing design. This is consistent with Remark 2: the law yields an undamped Coulomb-friction oscillator in δ_j, with no mechanism to remove a residual δ_j once sensor noise and bias excite it. The damped reaching law, together with the observer, is therefore the main difference from [29]; GA tuning alone does not make that design viable in a sensed closed loop.

3.10 Discussion and limitations

The study is based on simulation only. The sensor and link models are representative but are not identified from a specific vehicle. The proposed controller is not the most accurate in nominal or mildly disturbed conditions, uses 2.4-2.9 % more induced-power energy than the most economical baselines, and is more sensitive than FOPID to link delay, because its translational disturbance estimate depends on timely position data. It does not handle thrust saturation explicitly, which caused its failure in the combined worst case, and no controller tolerated a 60 % loss of one motor. The stability proof covers each channel and the convergence of the sliding variables, while the cascade is verified numerically rather than proved globally. Hardware-in-the-loop validation, saturation-aware fault-tolerant allocation and a delay-compensated observer are the next steps. The switching gain of the roll/pitch group was designed for an observer-error bound of 6 rad/s^2, which is exceeded (10.16 rad/s^2) during gust and fault transients; in those intervals only ultimate boundedness is guaranteed.

4 Conclusion

This paper placed a GA-tuned PFOID-SMC in a sensing- and communication-aware closed loop with multi-rate, biased and noisy sensors, a lossy link and a sliding mode observer whose state, disturbance and fault estimates feed the equivalent control. The reaching law of the earlier PFOID-SMC was replaced by a damped law, which gives finite-time reaching, exponential convergence of the sliding variables and asymptotic (Mittag-Leffler) convergence of the tracking error; these properties were also verified numerically, except in the roll and pitch channels during gust and fault transients, where the observer error exceeded the design bound and only ultimate boundedness holds. Across 15 scenarios with five seeds and five equally tuned baselines, the proposed controller was not the most accurate in nominal

conditions (0.119 m against 0.071 m for FOPID). It was the most accurate under strong wind (0.134 m), under parametric uncertainty up to +30 % (0.179 m against at least 0.82 m for all baselines) and under 20-40 % motor faults (0.119-0.147 m), where it also isolated the faulty motor. Without the observer the same controller diverged, which shows that the sensing and estimation layer, rather than GA tuning alone, provides the robustness. Future work will test the controller on other UAV platforms, add saturation-aware fault-tolerant allocation and delay compensation, and validate the design in hardware-in-the-loop experiments.

Data Availability Statement

This study is based entirely on numerical simulation; no physical experimental data were collected. The simulation code, GA run files and logged signals used to produce every figure and table are available from the corresponding author on reasonable request.

Funding

This work was supported without any funding.

Conflicts of Interest

The authors declare no conflicts of interest.

AI Use Statement

The authors declare that no generative AI was used in the preparation of this manuscript.

Ethical Approval and Consent to Participate

Not applicable. This study is based purely on simulation and involves no human participants, human data or animals.

References

[1] Van Nguyen, C., & Nguyen, M. T. (2023, December). Design and simulation of PID-based control system for UAV quadcopters. In *International Conference on Advances in Information and Communication Technology* (pp. 146-153). Cham: Springer Nature Switzerland. [CrossRef]

[2] Shakhatreh, H., Sawalmeh, A. H., Al-Fuqaha, A., Dou, Z., Almaita, E., Khalil, I., ... & Guizani, M. (2019). Unmanned aerial vehicles (UAVs): A survey on civil applications and key research challenges. *IEEE Access, 7*, 48572-48634. [CrossRef]

[3] Mahony, R., Kumar, V., & Corke, P. (2012). Multirotor aerial vehicles: Modeling, estimation, and control of quadrotor. *IEEE robotics & automation magazine, 19*(3), 20-32. [CrossRef]

[4] Dalwadi, N., Deb, D., & Ozana, S. (2023). Dual observer based adaptive controller for hybrid drones. *Drones, 7*(1), 48. [CrossRef]

[5] Hassanalian, M., & Abdelkefi, A. (2017). Classifications, applications, and design challenges of drones: A review. *Progress in Aerospace sciences, 91*, 99-131. [CrossRef]

[6] Idrissi, M., Salami, M., & Annaz, F. (2022). A review of quadrotor unmanned aerial vehicles: Applications, architectural design and control algorithms. *Journal of Intelligent & Robotic Systems, 104*(2), 22. [CrossRef]

[7] Khalid, A., Mushtaq, Z., Arif, S., Zeb, K., Khan, M. A., & Bakshi, S. (2023). Control schemes for quadrotor UAV: taxonomy and survey. *ACM Computing Surveys, 56*(5), 1-32. [CrossRef]

[8] Hua, M. D., Hamel, T., Morin, P., & Samson, C. (2013). Introduction to feedback control of underactuated VTOLvehicles: A review of basic control design ideas and principles. *IEEE Control systems magazine, 33*(1), 61-75. [CrossRef]

[9] Ma'arif, A., Suwarno, I., Nur'aini, E., & Raharja, N. M. (2023, January). Altitude control of UAV quadrotor using PID and integral state feedback. In *BIO Web of Conferences* (Vol. 65, p. 07011). EDP Sciences. [CrossRef]

[10] Maaruf, M., Hamanah, W. M., & Abido, M. A. (2023). Hybrid backstepping control of a quadrotor using a radial basis function neural network. *Mathematics, 11*(4), 991. [CrossRef]

[11] Kim, J., Gadsden, S. A., & Wilkerson, S. A. (2019). A comprehensive survey of control strategies for autonomous quadrotors. *Canadian Journal of Electrical and Computer Engineering, 43*(1), 3-16. [CrossRef]

[12] Danesh, M., Jalalaei, A., & Derakhshan, R. E. (2023). Auto-landing algorithm for quadrotor UAV using super-twisting second-order sliding mode control in the presence of external disturbances. *International Journal of Dynamics and Control, 11*(6), 2940-2957. [CrossRef]

[13] Åström, K. J., & Hägglund, T. (2001). The future of PID control. *Control engineering practice, 9*(11), 1163-1175. [CrossRef]

[14] Shah, P., & Agashe, S. (2016). Review of fractional PID controller. *Mechatronics, 38*, 29-41. [CrossRef]

[15] Efe, M. Ö. (2011). Integral sliding mode control of a quadrotor with fractional order reaching dynamics. *Transactions of the Institute of Measurement and Control, 33*(8), 985-1003. [CrossRef]

[16] Izaguirre-Espinosa, C., Muñoz-Vázquez, A. J., Sánchez-Orta, A., Parra-Vega, V., & Castillo, P. (2016). Attitude control of quadrotors based on fractional

sliding modes: Theory and experiments. *IET Control Theory & Applications, 10*(7), 825-832. [CrossRef]

[17] Shi, X., Cheng, Y., Yin, C., Dadras, S., & Huang, X. (2019). Design of fractional-order backstepping sliding mode control for quadrotor UAV. *Asian Journal of Control, 21*(1), 156-171. [CrossRef]

[18] Labbadi, M., Boukal, Y., & Cherkaoui, M. (2020). Path following control of quadrotor UAV with continuous fractional-order super twisting sliding mode. *Journal of Intelligent & Robotic Systems, 100*(3-4), 1429-1451. [CrossRef]

[19] Pazooki, M., & Mazinan, A. H. (2018). Hybrid fuzzy-based sliding-mode control approach, optimized by genetic algorithm for quadrotor unmanned aerial vehicles. *Complex & Intelligent Systems, 4*(2), 79-93. [CrossRef]

[20] Kumar, S., & Dewan, L. (2023). Control the quadcopter using hybrid controller under the disturbed environment. In *Proceedings of the International Conference of Control, Dynamic Systems, and Robotics (CDSR'23)*, Paper No. 204. Ottawa: Avestia. [CrossRef]

[21] Kumar, S., & Dewan, L. (2023). Quadcopter stabilization using hybrid controller under mass variation and disturbances. *Journal of Vibration and Control, 29*(21-22), 4857-4874. [CrossRef]

[22] Abro, G. E. M., & Abdallah, A. M. (2025). A synergistic fractional-order control for precise helical trajectory tracking and formation stability in multi-agent quadrotor uavs. *Arabian Journal for Science and Engineering, 50*(8), 6121-6140. [CrossRef]

[23] Nguyen, C. V., Nguyen, M. T., Tran, H. T., Trinh, M. L., La, H. M., & Nguyen, H. T. (2024). Trajectory tracking control for a quadcopter under external disturbances. *Engineering, Technology & Applied Science Research, 14*(6), 17620-17628. [CrossRef]

[24] Jijun, S., & Daogang, P. (2024). Application research on improved genetic algorithm and active disturbance rejection control on quadcopters. *Measurement and Control, 57*(9), 1347-1357. [CrossRef]

[25] Li, K., Bai, Y., & Zhou, H. (2024). Research on quadrotor control based on genetic algorithm and particle swarm optimization for pid tuning and fuzzy control-based linear active disturbance rejection control. *Electronics, 13*(22), 4386. [CrossRef]

[26] Derafa, L., Benallegue, A., & Fridman, L. (2012). Super twisting control algorithm for the attitude tracking of a four rotors UAV. *Journal of the Franklin Institute, 349*(2), 685-699. [CrossRef]

[27] Brahim, K. S., El Hajjaji, A., Terki, N., & Alabazares, D. L. (2023). Finite time adaptive SMC for UAV trajectory tracking under unknown disturbances and actuators constraints. *IEEE Access, 11*, 66177-66193. [CrossRef]

[28] Khaled, T., & Boumehraz, M. (2023). Adaptive sliding mode controller and observer for altitude and attitude control of a quadrotor. *arXiv preprint arXiv:2308.00572*. [CrossRef]

[29] Kumar, S., & Dewan, L. (2022). PFOID-SMC approach to mitigate the effect of disturbance and parametric uncertainty on the quadcopter. *International Journal of Modelling, Identification and Control, 40*(4), 343-355. [CrossRef]

[30] Hespanha, J. P., Naghshtabrizi, P., & Xu, Y. (2007). A survey of recent results in networked control systems. *Proceedings of the IEEE, 95*(1), 138-162. [CrossRef]

[31] Jin, G. G., Pal, P., Chung, Y. K., Kang, H. K., Yetayew, T. T., & Bhakta, S. (2023). Modelling, control and development of GUI-based simulator for a quadcopter using nonlinear PID control. *Australian Journal of Electrical and Electronics Engineering, 20*(4), 387-399. [CrossRef]

[32] Tripathi, V. K., Kamath, A. K., Behera, L., Verma, N. K., & Nahavandi, S. (2020). Finite-time super twisting sliding mode controller based on higher-order sliding mode observer for real-time trajectory tracking of a quadrotor. *IET Control Theory & Applications, 14*(16), 2359-2371. [CrossRef]

[33] Thanh, H. L. N. N., & Hong, S. K. (2018). Quadcopter robust adaptive second order sliding mode control based on PID sliding surface. *IEEE Access, 6*, 66850-66860. [CrossRef]

[34] Mian, A. A., & Daobo, W. (2008). Modeling and backstepping-based nonlinear control strategy for a 6 DOF quadrotor helicopter. *Chinese Journal of Aeronautics, 21*(3), 261-268. [CrossRef]

[35] Bouabdallah, S., & Siegwart, R. (2005, April). Backstepping and sliding-mode techniques applied to an indoor micro quadrotor. In *Proceedings of the 2005 IEEE international conference on robotics and automation* (pp. 2247-2252). IEEE. [CrossRef]

[36] Das, A., Lewis, F. L., & Subbarao, K. (2011). Sliding mode approach to control quadrotor using dynamic inversion. *Challenges and paradigms in applied robust control*, 3-24. [CrossRef]

[37] Ahmadi, K., Asadi, D., Merheb, A., Nabavi-Chashmi, S. Y., & Tutsoy, O. (2023). Active fault-tolerant control of quadrotor UAVs with nonlinear observer-based sliding mode control validated through hardware in the loop experiments. *Control Engineering Practice, 137*, 105557. [CrossRef]

[38] Emran, B. J., & Najjaran, H. (2018). A review of quadrotor: An underactuated mechanical system. *Annual Reviews in Control, 46*, 165-180. [CrossRef]

[39] Davila, J., Fridman, L., & Levant, A. (2005). Second-order sliding-mode observer for mechanical systems. *IEEE transactions on automatic control, 50*(11), 1785-1789. [CrossRef]

[40] Moreno, J. A., & Osorio, M. (2012). Strict Lyapunov functions for the super-twisting algorithm. *IEEE transactions on automatic control, 57*(4), 1035-1040. [CrossRef]

[41] Levant, A. (2003). Higher-order sliding modes, differentiation and output-feedback control. *International journal of Control, 76*(9-10), 924-941. [CrossRef]

[42] Monje, C. A., Vinagre, B. M., Feliu, V., & Chen, Y. (2008). Tuning and auto-tuning of fractional order controllers for industry applications. *Control engineering practice, 16*(7), 798-812. [CrossRef]

[43] Ayad, R., Nouibat, W., Zareb, M., & Bestaoui Sebanne, Y. (2019). Full control of quadrotor aerial robot using fractional-order FOPID. *Iranian Journal of Science and Technology, Transactions of Electrical Engineering, 43*(Suppl 1), 349-360. [CrossRef]

[44] Goldberg, D. E. (1989). *Genetic Algorithms in Search, Optimization, and Machine Learning*. Reading, MA: Addison-Wesley. https://dl.acm.org/doi/10.5555/534133

[45] Eker, I. (2006). Sliding mode control with PID sliding surface and experimental application to an electromechanical plant. *ISA transactions, 45*(1), 109-118. [CrossRef]

[46] Eker, I. (2010). Second-order sliding mode control with experimental application. *ISA transactions, 49*(3), 394-405. [CrossRef]

[47] Oustaloup, A., Levron, F., Mathieu, B., & Nanot, F. M. (2000). Frequency-band complex noninteger differentiator: characterization and synthesis. *IEEE Transactions on circuits and systems I: Fundamental theory and applications, 47*(1), 25-39. [CrossRef]

[48] Khalil, H. K. (2002). *Nonlinear Systems* (3rd ed.). Upper Saddle River, NJ: Prentice Hall. https://flyingv.ucsd.edu/krstic/files/Khalil-3rd.pdf

[49] Matignon, D. (1996, July). Stability results for fractional differential equations with applications to control processing. In *Computational engineering in systems applications* (Vol. 2, No. 1, pp. 963-968). https://www.researchgate.net/publication/2581881

[50] Li, Y., Chen, Y., & Podlubny, I. (2009). Mittag–Leffler stability of fractional order nonlinear dynamic systems. *Automatica, 45*(8), 1965-1969. [CrossRef]

[51] U.S. Department of Defense. (1980). *MIL-F-8785C: Military Specification, Flying Qualities of Piloted Airplanes*. Washington, DC. Retrieved from https://everyspec.com/MIL-SPECS/MIL-SPECS-MIL-F/MIL-F-8785C_5295/

[52] Podlubny, I. (1999). Fractional-order systems and $PI^{\lambda}D^{\mu}$-controllers. *IEEE Transactions on Automatic Control, 44*(1), 208-214. [CrossRef]

[53] Shtessel, Y., Edwards, C., Fridman, L., & Levant, A. (2014). *Sliding mode control and observation* (Vol. 10, pp. 978-970). New York: Birkhäuser. [CrossRef]



Nidhi Singh is an Assistant Professor in the Department of Electrical Engineering, Gautam Buddha University, Greater Noida, India. Her research is in control engineering, and her interests include controller design, control theory, distributed systems, MATLAB-based simulation and renewable energy. (Email: nidhi@gbu.ac.in)



Prashant Nigam received the B.Tech. degree in electrical and electronics engineering from Guru Gobind Singh Indraprastha University, India, in 2009, and the M.Tech. degree in digital communication from the Ambedkar Institute of Advanced Communication Technologies & Research (now NSUT East Campus), India, in 2011. He is pursuing the Ph.D. degree in the Department of Electrical Engineering, Gautam Buddha University, Greater Noida, India, working on controller design for nonlinear control systems. (Email: prashantnigs108@gmail.com)



Lillie Dewan received the Ph.D. degree from Kurukshetra University, Kurukshetra, India, in 2001. She is a Professor in the Department of Electrical Engineering, National Institute of Technology Kurukshetra, India. Her research interests include adaptive and robust control, instrumentation and biomedical signal processing. She has published 70 research articles in international journals and more than 80 papers in international conferences, and has supervised 17 Ph.D. and more than 40 M.Tech. students. (Email: l_dewan@nitkkr.ac.in)